

Extinction and dust/gas ratio in LMC molecular clouds

K. Dobashi^{1,2}, J.-P. Bernard¹, A. Hughes^{3,4}, D. Paradis¹, W. T. Reach⁵, and A. Kawamura⁶

¹ Centre d'Étude Spatiale des Rayonnements, CNRS, 9 Avenue du Colonel Roche, 31028 Toulouse, France
e-mail: dobashi@u-gakugei.ac.jp

² Department of Astronomy and Earth Sciences, Tokyo Gakugei University, Koganei, Tokyo 184-8501, Japan

³ Centre for Supercomputing and Astrophysics, Swinburne University of Technology, Hawthorn VIC 3122, Australia

⁴ CSIRO Australia Telescope National Facility, PO Box 76, Epping NSW 1710, Australia

⁵ IPAC/Caltech, MS 220-6, Pasadena, CA 91125, USA

⁶ Nagoya University, Dept. of Astrophysics, Chikusa-Ku, Nagoya, 464-8602, Japan

Received 27 November 2007 / Accepted 3 March 2008

ABSTRACT

Aims. The goal of this paper is to measure the dust content and distribution in the Large Magellanic Cloud (LMC) by comparing extinction maps produced in the near-infrared wavelengths and the spatial distribution of the neutral and molecular gas, as traced by HI and CO observations.

Methods. In order to derive an extinction map of the LMC, we have developed a new method to measure the color excess of dark clouds, using the 2MASS all-sky survey. Classical methods to measure the color excess (including the NICE method) tend to underestimate the true color excess if the clouds are significantly contaminated by unreddened foreground stars, as is the case in the LMC. We propose a new method that uses the color of the X percentile reddest stars and which is robust against such contamination. Using this method, it is possible to infer the positions of dark clouds with respect to the star distribution by comparing the observed color excess as a function of the percentile used and that predicted by a model.

Results. On the basis of the resulting extinction map, we perform a correlation analysis for a set of dark molecular clouds. Assuming similar infrared absorption properties for the dust in the neutral and molecular phases, we derive the absorption-to-column density ratio $\frac{A_V}{N_{\text{H}}}$ and the CO-to-H₂ conversion factor X_{CO} . We show that $\frac{A_V}{N_{\text{H}}}$ increases from the outskirts of the LMC towards the 30 Dor star-forming region. This can be explained either by a systematic increase of the dust abundance, or by the presence of an additional gas component not traced by HI or CO, but strongly correlated to the HI distribution. If dust abundance is allowed to vary, the derived X_{CO} factors for the selected regions are several times lower than those derived from a virial analysis of the CO data. This could indicate that molecular clouds in the LMC are not gravitationally bound, or that they are bounded by substantial external pressure. However, the X_{CO} values derived from absorption can be reconciled with the virial results assuming a constant value for the dust abundance and the existence of an additional, unseen gas component. These results are in agreement with those derived for the LMC from diffuse far-infrared emission.

Key words. ISM: dust, extinction – galaxies: Magellanic Clouds – infrared: ISM

1. Introduction

Studying dust in the Large Magellanic Cloud (LMC) is important for several reasons.

As the metallicity in the LMC is low, $Z \approx 0.3\text{--}0.5 Z_{\odot}$ (Westerlund 1997), the dust abundance in the LMC is expected to be lower than in the Milky Way (MW), although the relationship between dust abundance and metallicity is not yet firmly established. This is important for extragalactic studies, since the metallicity of the LMC is similar to that of galaxies at redshifts $z \sim 1$, when most of the Universe's star formation occurred. Not only the absolute dust abundance, but also the relative abundance of dust species is different in low-metallicity environments with respect to MW values (e.g., Galliano et al. 2003); this applies in particular to the smallest species such as Polycyclic Aromatic Hydrocarbons (PAH) and Very Small Grains (VSGs), which are responsible for most of the near to mid-infrared emission in galaxies. Variations in the dust composition will modify the Spectral Energy Distribution (SED) of a galaxy's infrared (IR) emission, with potentially significant consequences for the interpretation of cosmological IR surveys. In the MW, the relative abundance of these species is known to vary widely from region to region (e.g.,

Boulanger et al. 1990; Miville-Deschênes et al. 2002), but the origins of these variations are not always understood, and it is therefore unclear if similar variations will affect the global SED of low-metallicity galaxies. Similarly, the optical properties of the largest dust grains (Big Grains, BGs) are known to vary significantly between the diffuse atomic interstellar medium (ISM) and the denser molecular regions (e.g., Bernard et al. 1999; Stepnik et al. 2003; Dupac et al. 2002; Dupac et al. 2003). Although low-metallicity systems tend to host less molecular material, the processes responsible for the observed variations in grain properties could also be taking place in low-metallicity galaxies. Studying the dust abundances, properties, and spatial variations in low-metallicity systems such as the LMC is therefore of prime importance for cosmology.

Understanding the impact of metallicity on dust properties would also provide an additional handle to constrain the processes at work in the life-cycle of dust. This would provide much-needed insight into the influence of star formation activity on the dust formation and destruction, the effect of dust abundance on the formation of molecules such as H₂, the effectiveness of tracers of the molecular phase such as CO, the efficiency of dust destruction processes in the warm diffuse ISM,

and dust aggregation in dense clouds. Another outstanding topic under investigation is the possibility that a significant fraction of the mass of low metallicity galaxies might be locked in a phase where H_2 has formed (and self-shielding), but CO is photodissociated.

Due to its proximity (LMC ≈ 50 kpc, Keller & Wood 2006; Feast 1999), the LMC offers a unique opportunity to study the spatial distribution of dust in a low-metallicity environment. Following the large-scale, low angular resolution surveys by IRAS and DIRBE (e.g., Sauvage et al. 1990; Sakon et al. 2006), recent systematic, higher angular resolution IR observations of the LMC and SMC conducted by Spitzer (see Meixner et al. 2006; Bernard et al. 2008; Bot et al. 2004) and Akari now permit the efficient separation of the diffuse emission from that of point sources. This is an important prerequisite for understanding the physics of dust emission, since the emission depends strongly on the intensity of the local interstellar radiation field (ISRF) and on the relative distribution of dust and stars. An additional advantage of the LMC is the galaxy’s almost face-on orientation. This provides a complete view of the gas distribution that is almost independent of the interpretation of velocity information, and allows us to study the dust emission with almost no confusion between regions along the line of sight.

In addition to the limitations imposed by variations of the dust abundance and/or optical properties of dust, dust emission is also roughly proportional to the strength of the local ISRF, which is generally unknown. To some extent, this limitation can be overcome when the temperature of the large dust grains is known through the SED at far-infrared (FIR) wavelengths, but this is only rarely the case with presently available FIR data. In the MW, studies of the extinction due to dust in the optical and near-infrared (NIR) have been very useful to circumvent this limitation, primarily because extinction arises from the same grains that produce the FIR emission, whereas extinction is independent of the radiation field intensity. Comparing the extinction with the FIR emission constrains the optical properties of dust and their spatial variations (Cambr sy et al. 2005). Unlike emission, extinction properties of dust are unlikely to be strongly affected by the phase of the ISM, in particular in the NIR where grain size effects are small.

Large scale extinction maps of the Galactic plane and Galactic structure have been obtained from optical star counts (e.g., Dobashi et al. 2005; Cambr sy 1999) as well as from measurements of the near-infrared color excess (e.g., Lombardi & Alves 2001). However, constructing extinction maps of the LMC has proved more difficult, partly because the dust extinction is smaller than in the Galaxy, but mostly because the intrinsic stellar density distribution is harder to model and color distributions also change systematically within the LMC’s stellar bar.

In this paper, we derive a map of the visual extinction (A_V) in the LMC using the 2 Micron All-Sky Survey (2MASS) point source catalog. We use a new technique that we have developed from the Near-Infrared Color Excess (NICE) method originally introduced by Lada et al. (1994), which utilizes the reddening of the background stars behind dark clouds. The NICE method, like the improved NICER method (Lombardi & Alves 2001), quantifies the color excess due to dark clouds by measuring the difference between the mean color of stars towards dark clouds and reference fields (i.e., cloud-free regions). The method therefore tends to underestimate the true extinction when the clouds are contaminated by unreddened foreground stars, although it works well for nearby Galactic dark clouds with low foreground contamination (e.g., Alves et al. 1998; Cambr sy et al. 2002). A better estimate of the dust extinction can be obtained if it is

possible to identify foreground stars and remove them from the sample of stars used. For dark clouds in the LMC however, it is not easy to distinguish foreground stars because the color excess caused by the clouds is much smaller than for nearby Galactic clouds, and the color excess is comparable to the intrinsic dispersion of stellar colors. Furthermore, the observable dark clouds in the LMC are Giant Molecular Clouds (GMCs), so there will be a large number of stars located inside the clouds themselves, which should be taken into account when deriving the color excess. It is important to note that in the case of dark clouds in the LMC, the simple NICE or NICER method can only work properly if sources located completely beyond the LMC, such as distant galaxies, are used.

In the new method described in this paper, we use all of the stars observed toward the LMC dark clouds, taking into account the intrinsic dispersion of star colors as well as the contribution of stars in the foreground and within the clouds. The basic idea is to measure the color excess based on a simple geometrical model of a cloud’s position relative to the star distribution in the LMC. Our new method therefore provides an estimate of the true color excess as well as the location of clouds with respect to the stellar distribution in the LMC through a comparison with model calculations.

The purpose of this paper is to generate an A_V extinction map of the LMC using the 2MASS point source catalog, and then to compare it to atomic and molecular gas tracers in order to measure the gas-to-dust ratio, $\frac{A_V}{N_{\text{H}}}$, and the X_{CO} factor. In Sect. 2, we present our new method to measure the color excess of dark clouds on the basis of the 2MASS point source catalog, and describe how the resulting color excess map is converted into a map of the visual extinction, A_V . In Sect. 3, we perform a correlation analysis of the dust extinction and gas emission (HI and CO) from a sample of LMC dark clouds, and we discuss the results in Sect. 4.

2. Extinction map of the LMC

We first describe a simple model of a dark cloud in the LMC to explain our new method to measure the color excess. The key is to utilize the color of the X percentile reddest star falling in a cell, rather than the simple mean star color in the cell. We demonstrate that the new method can determine the position of a dark cloud relative to the distribution of stars, and we compare our derived A_V map with the optical data presented by Zaritsky et al. (2004).

2.1. Method and model to measure the color excess

In the NICE method, one defines cells around the dark clouds, and measures the difference between the “typical” colors of stars falling in the cells within the dark clouds and in a reference field, assumed to be free of extinction. In the traditional NICE method, the typical color is usually chosen to be the mean color of stars in each cell. Cambr sy et al. (2002) proposed the median color of stars instead of the mean color, since it is less affected by the foreground contamination. In the method proposed here, we first sort the stars in each cell according to their colors (from blue to red), and then define the typical color as the color of the X_0 percentile reddest star (i.e. $X_0 = 100\%$ denotes the reddest star). We define a second typical color by taking the mean color of stars in the range $[X_0, X_1]$ percentile where $X_0 < X_1$. We refer to these two typical colors as C_{X_0} and C_{X_m} respectively. If there are N stars in a given cell, and the color of the i th star (after

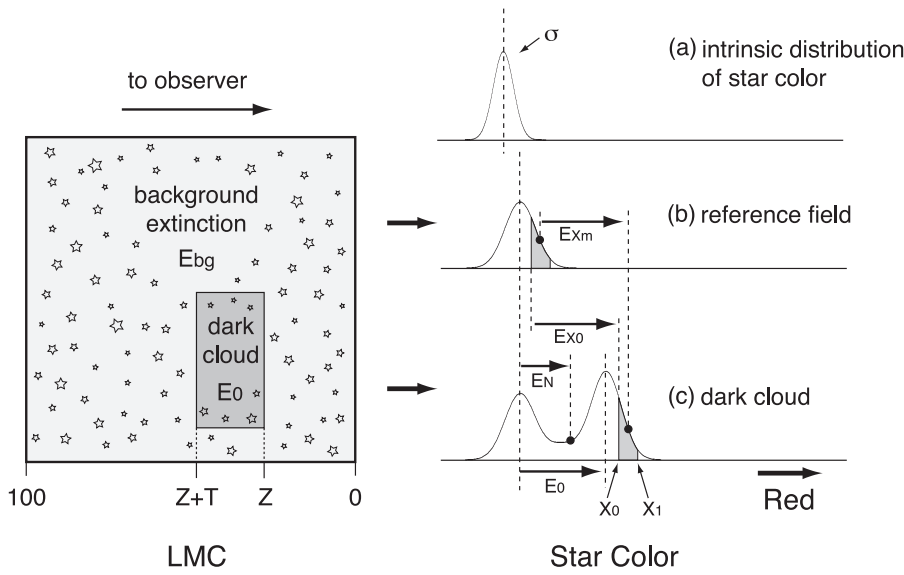


Fig. 1. Schematic illustration of the model used to estimate the color excess caused by a dark cloud in the LMC. (*Left*) We set uniform background extinction and locate a dark cloud within the LMC. The position and thickness of the cloud are taken to be $Z\%$ and $T\%$ of the total thickness of the LMC along the line of sight to the observer. E_{bg} and E_0 are the total color excess caused by the background and the cloud, respectively. (*Right*). In panel **a**), we generate a number of stars which have an intrinsic color distribution that follows a Gaussian distribution with a standard deviation σ , and we distribute the stars randomly in the LMC including the inner region of the cloud. The color distributions shown in panels **b**) and **c**) are the reddened distributions observed toward the reference field (i.e., a cloud-free region) and the dark cloud, respectively. E_{X_0} and E_{X_m} are the color excesses measured using Eqs. (3) and (4), and E_N is the color excess measured by the classical methods using either the simple mean or median color of the stars.

sorting from blue to red) is expressed as $c(i)$ with $i = 1 - N$, these two typical colors can be expressed as,

$$C_{X_0} = c(N_0) \quad (1)$$

$$C_{X_m} = \frac{1}{N_1 - N_0 + 1} \sum_{i=N_0}^{N_1} c(i), \quad (2)$$

where N_j for $j = 0$ and 1 is the half-adjusted integer of $\frac{X_j}{100}N$. We call the color excesses measured using these colors E_{X_0} and E_{X_m} , i.e.,

$$E_{X_0} = C_{X_0} - \bar{C}_{X_0} \quad (3)$$

$$E_{X_m} = C_{X_m} - \bar{C}_{X_m}, \quad (4)$$

where \bar{C}_{X_0} and \bar{C}_{X_m} are the typical colors in the reference field. In addition to measuring the color excess, we define E_N as the color excess measured by the mean star color (the NICE method) or the median star color (the method of [Cambr esy et al. 2002](#)), which correspond to our E_{X_m} for $(X_0, X_1) = (0, 100)\%$ and E_{X_0} for $X_0 = 50\%$, respectively. The three color excesses E_{X_0} , E_{X_m} , and E_N should agree if all of the stars are located in the background of dark clouds and if the intrinsic dispersion of star color is negligible compared to the color excess caused by the clouds. Such assumptions are not realistic for dark clouds in the LMC. In general, E_{X_m} is the closest to the true color excess E_0 and the relation $E_0 \geq E_{X_m} \geq E_{X_0} \geq E_N$ holds at high X_0 and X_1 values.

In order to evaluate the variation between the different estimates for the color excess (E_0 , E_{X_m} and E_N), we propose a simple model. As illustrated in Fig. 1, we assume that the LMC is filled with a uniform background extinction corresponding to the total color excess E_{bg} . We then position a dark cloud with extinction corresponding to the color excess E_0 within the LMC. In other words, a star beyond the LMC is observed to be reddened by E_{bg} in the reference field, and by $E_{\text{bg}} + E_0$ within the cloud. The position and the thickness of the cloud are set to Z and T percent of the total thickness of LMC along the line of sight. If we assume that the intrinsic color variation of stars in the LMC follows a Gaussian distribution with a standard deviation σ (Fig. 1a), stars should be observed to be reddened by a

maximum of E_{bg} in the reference field (Fig. 1b), and by $E_{\text{bg}} + E_0$ in the cloud (Fig. 1c). In Fig. 1, we illustrate the qualitative relations between the true color excess of the cloud E_0 , the color excess measured by the classical methods E_N , and the color excesses determined using our method (E_{X_0} and E_{X_m}).

For the model described above, we performed a simulation distributing stars randomly along the line-of-sight extent of the LMC to calculate E_{X_0} and E_{X_m} as a function of X_0 for various sets of parameters σ , E_{bg} , E_0 , Z , T , and X_1 . In Fig. 2, we show some results of these calculations for different values of σ and E_{bg} , with common parameters $E_0 = 0.3$ mag, $Z = 30\%$, $T = 10\%$, and $X_1 = 95\%$. It is evident that when the dispersion of star colors σ is much smaller than the true color excess E_0 (Fig. 2a), both E_{X_0} and E_{X_m} are very close to the true color excess E_0 in the high X_0 range (e.g., $X_0 > 50\%$ in Fig. 2a). This is a scenario where the classical methods will work well. However, when σ is not negligible compared to E_0 (Fig. 2b), E_{X_m} and E_{X_0} will underestimate E_0 even at a high X_0 values. For example, E_{X_m} at $X_0 = 80\%$ in Fig. 2b underestimates E_0 by $\approx 10\%$, although it gives a much better estimate than the value derived from the classical methods, which corresponds to E_{X_0} at $X_0 = 50\%$ or E_{X_m} at $X_0 = 5\%$. It is worth noting that the presence of a background color excess E_{bg} improves the estimate of E_0 : For example, if we use the same parameters as in Fig. 2b and change only the background E_{bg} from 0 to 0.25 mag, E_{X_m} and E_{X_0} at $X_0 > 70\%$ give better estimates of E_0 (Fig. 2c). This is because E_{bg} changes the shapes of the profiles of star colors in the reference field and in the dark cloud (Figs. 1b and c), which the measurements of E_{X_m} and E_{X_0} depend on.

The actual parameters of clouds in the LMC are similar to those shown in Fig. 2c. The dispersion of star colors in $J - H$ and $H - K_S$ is approximately $\sigma \sim 0.1$ mag, and the color excesses E_0 and E_{bg} are only a few times larger than σ in the LMC. Moreover, as the LMC is almost face-on and the observable clouds are mostly GMCs, the dark clouds should occupy a large fraction of the LMC's total thickness along the line of sight ($T \sim 10\%$ or more). If we were able to observe the Cyg OB 7 complex in Cygnus, which has a linear size of ~ 50 pc (e.g., [Dobashi et al. 1994](#)), from outside the Galaxy, the model parameter T would amount to $\sim 25\%$, assuming the scale height of the Galaxy is 100 pc.

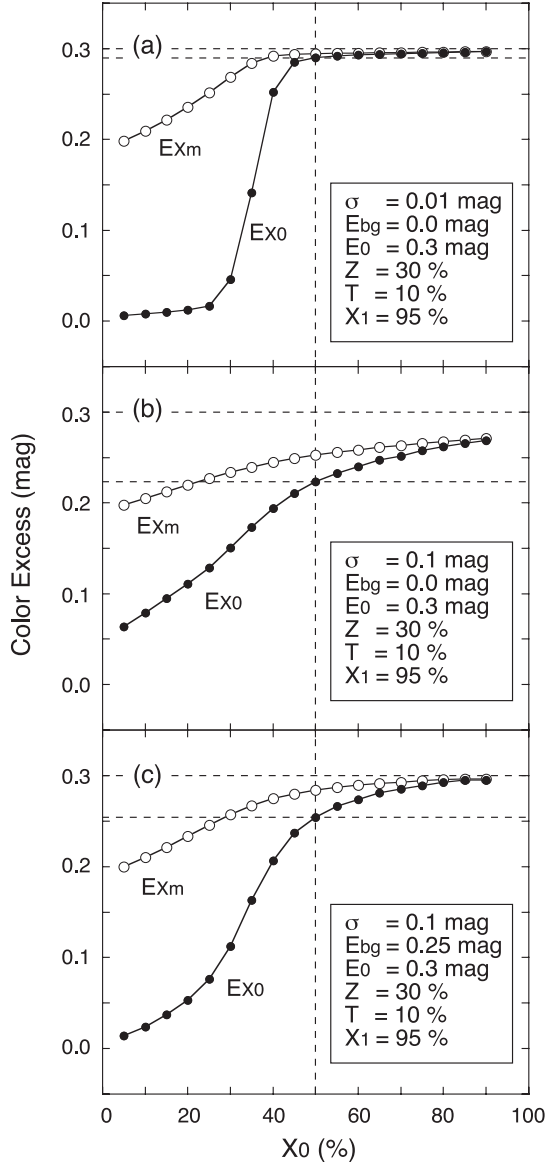


Fig. 2. Example of calculations using the model shown in Fig. 1. The true color excess, cloud position, and cloud thickness are set to $E_0 = 0.3$ mag, $Z = 30\%$, and $T = 10\%$ respectively. For a fixed value of $X_1 = 95\%$, E_{X_0} and E_{X_m} are calculated and shown as a function of X_0 . The intrinsic star color dispersion σ and the color excess due to the background extinction E_{bg} are set to **a)** $[\sigma, E_{bg}] = [0.01, 0.0]$ mag, **b)** $[0.1, 0.0]$ mag, and **c)** $[0.1, 0.25]$ mag. In each panel, the true color excess $E_0 = 0.3$ mag and the color excess E_{X_0} at $X_0 = 50\%$ are indicated by broken lines.

Our model is robust against contamination not only by foreground stars but also by intrinsically red sources, such as Young Stellar Objects (YSOs) and Asymptotic Giant Branch (AGB) stars. These sources can cause a serious overestimation of the true color excess. In the LMC, there are a number of YSOs forming in GMCs (e.g., Fukui et al. 2008), and AGB stars are known to be widely distributed (Tsalmantza et al. 2006). These intrinsically red sources, however, occupy only a small fraction of the 2MASS point sources in the LMC, and they can be removed by setting an appropriate X_1 value (e.g., $X_1 = 95\%$, see Sect. 2.3).

To summarize the results of our simulation, we find that E_{X_m} and E_{X_0} for high X_0 values derived using the percentile method trace the true color excess E_0 much better than the quantity E_N

measured by the classical methods. In the following subsections, we use our new method to construct maps of the color excess and extinction in the LMC. Foreground stars and stars inside dark clouds are accounted for in our model, and therefore the comparison between the observed E_{X_m}/E_{X_0} and the model calculations as a function of X_0 provide information about the position of individual clouds with respect to the star distribution in the LMC, through determining the best-fitting parameters T and Z .

2.2. Derivation of the extinction map

To derive a map of the visual extinction (A_V) in the LMC, we first measured the distribution of star colors using data in the 2MASS All-Sky Point Source Catalog, obtained from the Infrared Science Archive (IRSA) at the Infrared Processing and Analysis Center (IPAC). We selected stars that satisfy the following three criteria: (1) magnitudes brighter than 16.0, 15.5, and 15.0 mag in J , H , and K_S band respectively; (2) high-quality detections, photometry, and astrometry (i.e., the read flag “rd_flg” in the catalog is either 1, 2, or 3, and the photometry flag “ph_qual” is either A, B, or C for the 3 bands); and (3) no counterparts among known minor planets (i.e., the minor planet flag “mp_flg” is 0).

For criterion (1), the true magnitude limits for complete detection in the three bands vary from region to region in the LMC, and they are mostly lower than the threshold magnitudes that we have adopted. However, we use the threshold magnitudes stated above to increase the number of stars in each cell and to reduce the noise in the final extinction map. It is worth noting that as long as we use stars with photometry guaranteed by criterion (2), a slight change in the threshold magnitudes does not greatly influence the quality of the final extinction map, since the map is derived using star colors.

We placed circular cells with a diameter of $2'.6$ at a $1'$ grid spacing over the extent of the LMC, and then measured the typical colors ($J-H$ and $H-K_S$) of the selected stars falling in each cell at every 5 percentile in X_0 within the range $10\% \leq X_0 \leq 90\%$ with a common $X_1 = 95\%$. Here, the typical colors are C_{X_0} and C_{X_m} defined in Eqs. (1) and (2). As described in the next subsection, the rationale for using $X_1 = 95\%$ instead of $X_1 = 100\%$ is to avoid contamination by intrinsically red sources such as AGB stars and YSOs. The cell size that we have adopted is the same as the beam size of the NANTEN telescope ($HPBW = 2'.6$) in order to facilitate a direct comparison between the extinction map and the CO data obtained by NANTEN.

In order to determine the background star color distribution at a certain value of X_0 , we applied a median filter with a width of $1^\circ \times 1^\circ$ to the color maps C_{X_0} and C_{X_m} , and henceforth treat the resulting filtered maps as the background color distribution (i.e., \bar{C}_{X_0} and \bar{C}_{X_m} in Eqs. (3) and (4)). By substituting our typical color and background maps into Eqs. (3) and (4), we obtain color excess maps, $E_{X_0}(\lambda_1 - \lambda_2)$ and $E_{X_m}(\lambda_1 - \lambda_2)$, for each of the trial X_0 values. We assume that the color excess is proportional to the visual extinction, A_V . For a given reddening law ($\alpha_{\lambda_1} = A_{\lambda_1}/A_V$), the relationship between the color excess and A_V is expressed as,

$$A_{V X_k}^{\lambda_1 \lambda_2} = R_{\lambda_1 \lambda_2} E_{X_k}(\lambda_1 - \lambda_2) = \frac{1}{\alpha_{\lambda_1} - \alpha_{\lambda_2}} E_{X_k}(\lambda_1 - \lambda_2), \quad (5)$$

where $A_{V X_k}^{\lambda_1 \lambda_2}$ the visual extinction derived from $E_{X_k}(\lambda_1 - \lambda_2)$ for $k = 0$ or m .

Although Cambrésy et al. (2002) have shown that the reddening law in some Galactic clouds in Cygnus follows the relation given by Rieke & Rebofsky (1985) rather than the law

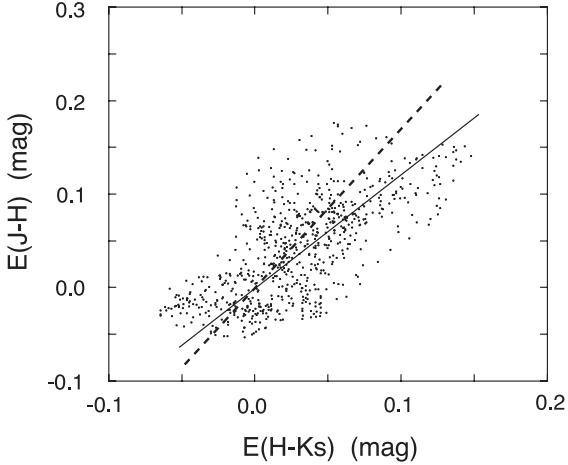


Fig. 3. Plot of $E(H - K_S)$ vs. $E(J - H)$ around the cloud LMC-154. The data values are E_{X_m} measured at $[X_0, X_1] = [80, 95]\%$. The reddening law suggested by Rieke & Rebofsky (1985) is shown by the broken line, and the reddening law suggested by Cardelli et al. (1989) for $R_V = 3.1$ is indicated by the solid line.

proposed by Cardelli et al. (1989), we found that the reddening law by the latter authors better represents the observed color-color diagram $E(H - K_S)$ vs. $E(J - H)$ for clouds in the LMC. As an example, Fig. 3 shows the relation between $E_{X_m}(H - K_S)$ and $E_{X_m}(J - H)$ at $X_0 = 80\%$ measured around the cloud LMC-154. This cloud is minimally contaminated by foreground stars, and it is well detected at this percentile (see Sect. 2.4). It is apparent from Fig. 3 that the relation suggested by Cardelli et al. (1989) with a ratio of total to selective extinction of $R_V = 3.1$ represents the actual data better than the relation suggested by Rieke & Rebofsky (1985), although the data points in the figure have a rather large dispersion. Gordon et al. (2003) have also shown that there is no significant difference in the reddening law at visible to near-infrared wavelengths in the Galaxy and the LMC, although there are clear differences in the ultraviolet for many lines of sight. Although the actual reddening law probably varies between locations in the LMC, we adopt the α_λ values found by Cardelli et al. (1989) with $R_V = 3.1$, which reduces Eq. (5) to

$$A_{VX_k}^{JH} = 10.9E_{X_k}(J - H) \quad (6)$$

$$A_{VX_k}^{HK} = 13.2E_{X_k}(H - K_S). \quad (7)$$

We use these equations to convert the color excess maps, $E_{X_k}(J - H)$ and $E_{X_k}(H - K_S)$, into the visual extinction maps $A_{VX_k}^{JH}$ and $A_{VX_k}^{HK}$.

The visual extinction derived using the coefficients in Eqs. (6) and (7) could be as much as ~ 3 times higher than the extinction derived from star counts at V band (for details, see Sect. 2.5), which suggests that the reddening law of Cardelli et al. (1989) may not accurately apply to the LMC at the wavelengths considered here. However, because it is clearly shown by Gordon et al. (2003) that the reddening law in the LMC is very similar to that suggested by Cardelli et al. (1989) in the visible to the near-infrared regime, we use Eqs. (6) and (7) in this paper. The coefficients in these equations should be rescaled when the reddening law in the LMC is better determined for near-infrared wavelengths.

In order to increase the signal to noise ratio (S/N) of the extinction map, we combined the $A_{VX_k}^{JH}$ and $A_{VX_k}^{HK}$ maps into one map, averaging them with a weight determined by their noise

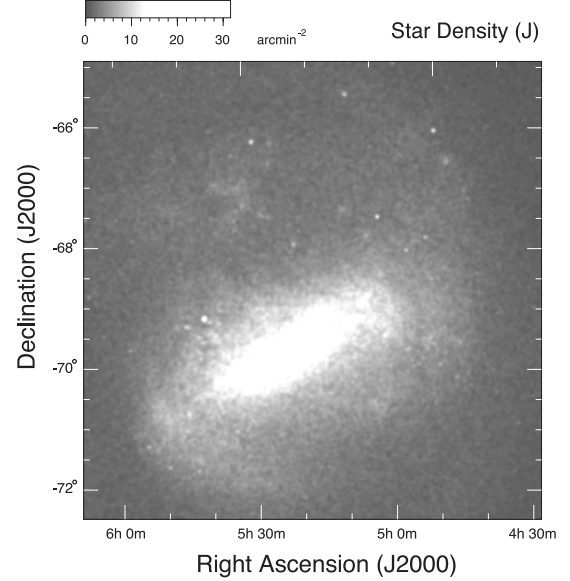


Fig. 4. Star density map of the LMC. The distribution of stars brighter than 16 mag in J band is shown in units of arcmin^{-2} .

levels $\delta A_{VX_k}^{JH}$ and $\delta A_{VX_k}^{HK}$. The noise varies from region to region in the maps, because the number of stars, N , used to measure the colors also varies. We show an example of the star density maps in Fig. 4. Typically, $N \sim 50$ – 100 stars are found per resolution element ($2''.6$) in the most opaque regions such as the 30 Dor complex and LMC-154, as well as in the outskirts of the LMC, while as many as $N \sim 500$ stars are found per resolution element in the central region. Due to such variations, the noise is higher at the edge of the maps where the star density is lower. The noise levels, however, cannot be estimated as a simple count uncertainty (i.e., $1/\sqrt{N}$), because A_V values in Eqs. (6) and (7) are not based on a simple mean of star colors as shown in Eqs. (1) and (2). In order to estimate the map noise levels $\delta A_{VX_k}^{JH}$ and $\delta A_{VX_k}^{HK}$ numerically, we performed a Monte-Carlo simulation. First, we generated a random set of as many stars as were actually observed in each cell, assuming that the star colors follow a Gaussian distribution with standard deviation σ . We then generated an extinction map for the simulated star catalog in the same way as for the actual data. We repeated the simulation 100 times, and took the standard deviation of the resulting A_V values in each cell as the noise levels $\delta A_{VX_k}^{JH}$ and $\delta A_{VX_k}^{HK}$. After several trials, we set the constant standard deviation of the star color σ used for the simulation to $\sigma = 0.22$ mag and 0.18 mag for the colors $J - H$ and $H - K_S$, which makes the resulting noise maps most similar to the actual noise levels.

Using the noise levels derived above, we combined the two extinction maps according to,

$$A_{VX_k} = \left[\frac{A_{VX_k}^{JH}}{(\delta A_{VX_k}^{JH})^2} + \frac{A_{VX_k}^{HK}}{(\delta A_{VX_k}^{HK})^2} \right] \left[\frac{1}{(\delta A_{VX_k}^{JH})^2} + \frac{1}{(\delta A_{VX_k}^{HK})^2} \right]^{-1}. \quad (8)$$

The noise level in the combined extinction map is given by,

$$\delta A_{VX_k} = \frac{\delta A_{VX_k}^{JH} \delta A_{VX_k}^{HK}}{\sqrt{(\delta A_{VX_k}^{JH})^2 + (\delta A_{VX_k}^{HK})^2}}. \quad (9)$$

In Fig. 5, we show one of the resulting extinction maps (A_{VX_m} at $X_0 = 80\%$) covering the entire region of the LMC. Although

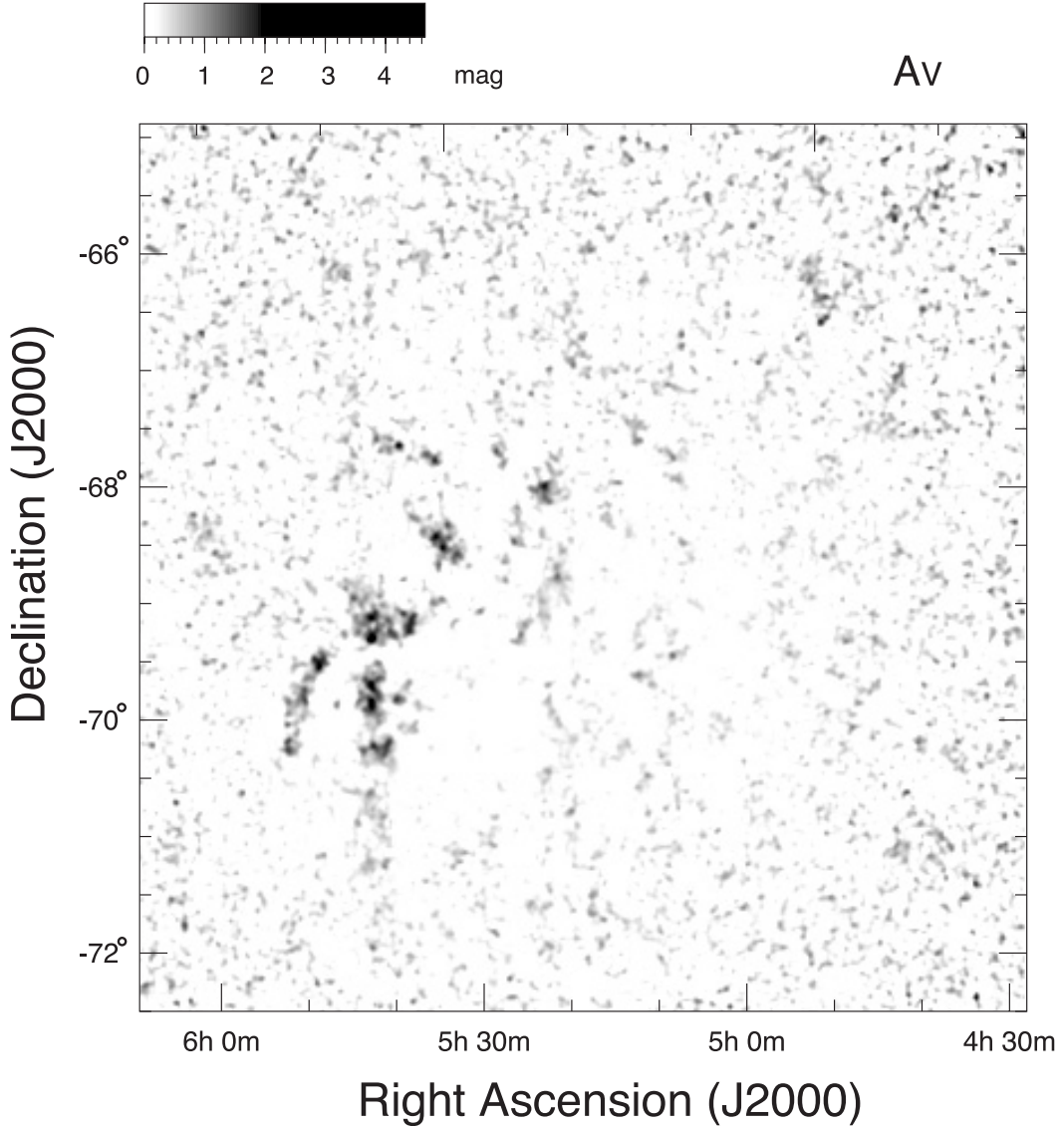


Fig. 5. Extinction map of A_V derived from $E_{X_m}^{JH}$ and $E_{X_m}^{HK}$ measured in the range $[X_0, X_1] = [80, 95]\%$. The angular resolution of the map is $2''.6$.

the map is still rather noisy, some well known clouds such as the 30 Dor complex, LMC-114, and LMC-154 (Fukui et al. 2008) are clearly detected. The CO arc discovered by Mizuno et al. (2001) using the NANTEN telescope is also seen. We show in Sect. 3 that there is a clear correlation between the extinction map derived here and the distribution of the HI and CO emission.

To illustrate how the extinction map depends on X_0 , Fig. 6 shows some A_{VX_m} maps around the 30 Dor region on a finer scale. These maps are generated using different X_0 values: $X_0 = 20, 50$, and 80% . As the figure shows, clouds are better detected in the A_{VX_m} maps generated using higher X_0 values. As we also might expect from Fig. 2, the A_{VX_m} maps trace the extinction better than A_{VX_0} maps (not shown), and both are more complete for higher X_0 values, with less underestimation of the true extinction. Overall, the two types of extinction maps, A_{VX_m} and A_{VX_0} , are in satisfactory agreement for X_0 greater than $\sim 70\%$.

The noise level in the extinction maps also varies with X_0 . The mean noise level, δA_{VX_m} , averaged over the entire extent of the map increases monotonically with X_0 from ~ 0.4 mag to ~ 0.6 mag, while that of δA_{VX_0} remains in the range ~ 0.4 – 0.7 mag with a minimum around $X_0 \sim 50\%$. For the

extinction maps derived here, the A_{VX_m} maps in the high X_0 range ($>70\%$) have a moderate noise level and should trace the true extinction best. In the next section, we compare the emission from various gas tracers (CO, HI and H_α) with the A_{VX_m} map at $X_0 = 80\%$. For the rest of this paper, we refer to the A_{VX_m} map measured at this percentile as “the A_V map”.

2.3. Contamination by AGB stars and YSOs

Here we consider the possible influence of AGB stars and YSOs in our estimate of the extinction. These objects are known to have intrinsically red colors that could lead color-excess methods to overestimate extinction.

Tsalmantza et al. (2006) searched for AGB stars in nearby galaxies based on the 2MASS point source catalog, and they identified 7137 AGB star candidates in the LMC. Following Davidge (2003), they defined AGB stars as sources having colors $H - K_S > 0.4$ mag and $J - K_S > 1.5$ mag. Figure 7a displays the color-color diagram of the 588 444 stars found in the entire region shown in Fig. 5. Among these, we find that 6597 sources can be classified as AGB stars falling in the color region defined

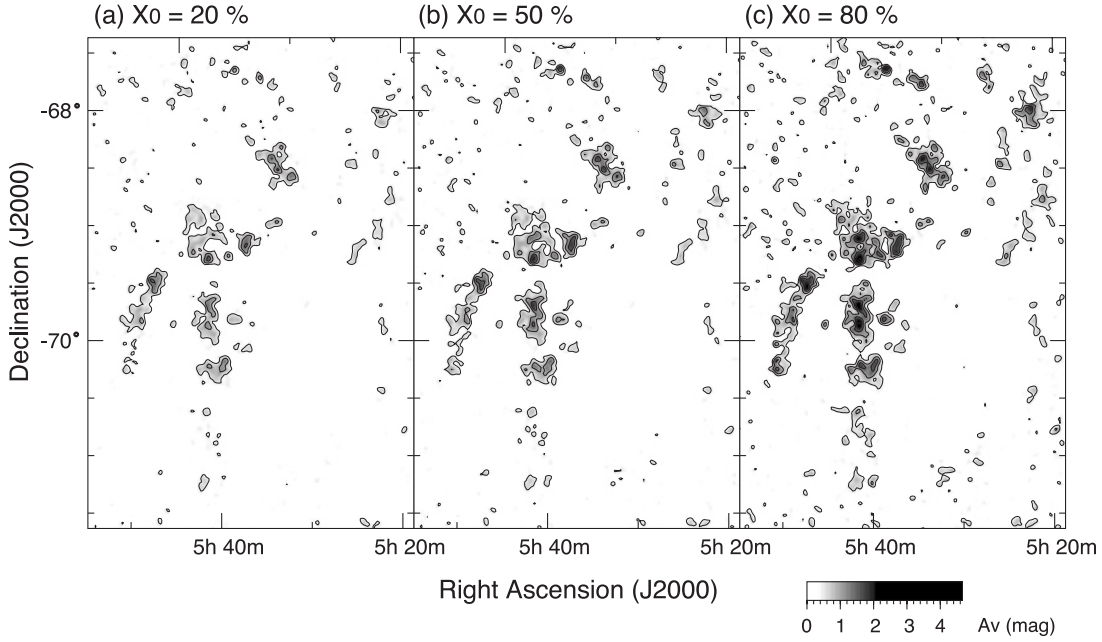


Fig. 6. Sample of the extinction maps derived from E_{X_m} at different X_0 values: for a fixed value of $X_1 = 95\%$, the maps in panels **a**), **b**), and **c**) are calculated for $X_0 = 20, 50$, and 80% respectively. In all panels, the lowest contour and the contour interval are set to $A_V = 0.5$ mag.

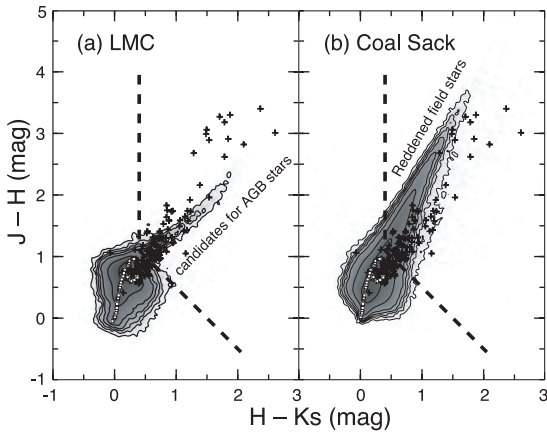


Fig. 7. **a**) Color-color diagram of 588 444 stars in the LMC found in the entire region of Fig. 5. Contours represent the point density in logarithmic scale starting from $\log\left(\frac{N}{\text{mag}^2}\right) = 0.5$ with a step of 1.0. For comparison, colors of the YSOs found in the Taurus region (Luhman et al. 2006) and the unreddened field stars (i.e., dwarfs and giant sequences, Bessell & Brett 1988) are indicated with plus signs and open squares, respectively. The broken line denotes the boundary of the color region for AGB stars defined by $H - K_S > 0.4$ mag and $J - K_S > 1.5$ mag (see text). **b**) same as **a**), but for 2 041 151 stars in the Coal Sack region in the Milky Way ($l = 300^\circ \sim 306^\circ$ and $b = -4^\circ \sim 3^\circ$), where most of red stars are field stars reddened by strong interstellar extinction.

by $H - K_S > 0.4$ mag and $J - K_S > 1.5$ mag, which is delineated by the broken line in Fig. 7a. This number is close to that found by Tsalmantza et al. (2006), though there is a slight difference due to the different selection criteria of stars used in our and their studies. For comparison, we plot in the figure the YSOs in the Taurus region (Luhman et al. 2006) as well as the unreddened field stars (i.e., dwarfs and giants; Bessell & Brett 1988). We also show in Fig. 7b the color-color diagram of sources in

the Coal Sack region in the MW where most of the field stars are reddened by the strong interstellar extinction.

As can be seen in Fig. 7, AGB stars, YSOs, and reddened field stars have slightly different colors. However, it is difficult to classify all of them reliably based only on the colors, because their difference in the diagram is small especially in low extinction regions (e.g., around $H - K_S \sim 0.6$ and $J - H \sim 1.1$ mag in Fig. 7). If we adopt the criteria of Tsalmantza et al. (2006) to eliminate AGB stars from our sample to derive the extinction maps, most of the YSOs and reddened field stars – in addition to the AGBs – would be excluded, leading to an underestimation of the true A_V . We therefore did not attempt to exclude AGB stars or YSOs based on their colors, but rather by setting X_1 in Eqs. (1) and (2) to 95%. This should be effective, because such intrinsically red sources are only a small fraction of our sample. As noted above, only $\sim 1.1\%$ of the 2MASS sources in the LMC (6597 of 588 444) are classified as AGB stars. The fraction of such sources increases towards higher extinction regions: in regions with $A_V > 1$ mag in our A_V map, there are 17 550 sources in total, of which 482 ($\sim 2.7\%$) can be classified as AGB stars, and the fraction increases to $\sim 3.4\%$ (34 of 988 sources) in denser regions with $A_V > 2$ mag. This trend is probably due to YSOs forming in the clouds, because the criteria for the AGB stars is not sufficient to exclude YSOs.

In any case, the fraction of the sources located on the right side of the broken line in Fig. 7a (AGB stars, YSOs, and reddened field stars) is no more than a few percent throughout the LMC, and therefore nearly all of them should be excluded by setting $X_1 = 95\%$ when deriving the A_V maps. We note, however, that there must also be some YSOs on the left side of the broken line in Fig. 7a. These are potentially a source of overestimation of A_V , especially if clustered. Clusters of YSOs can often be recognized as a compact region in clouds having a very red mean color and a high star density (e.g., Cambrésy et al. 2002). Towards the clouds detected in our A_V map, we searched for pixels having larger A_V (i.e., color excess) and higher star

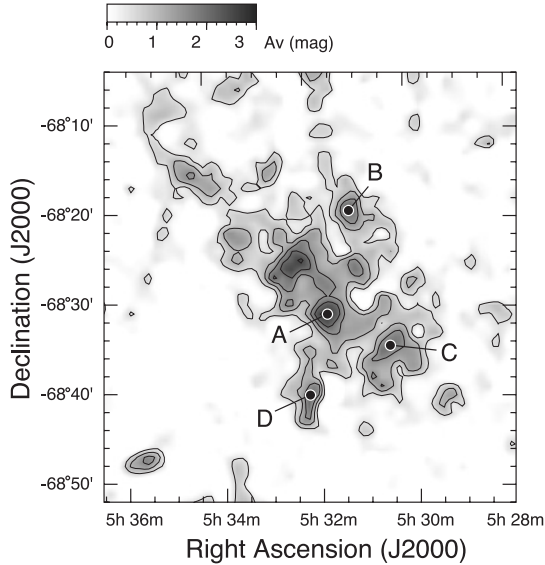


Fig. 8. Extinction map around the cloud LMC-154 derived from E_{X_m} for $[X_0, X_1] = [80, 95]\%$. The lowest contour and the contour interval are $A_V = 0.5$ mag. Labels “A”–“D” mark the positions where the data shown in Fig. 10 are sampled.

density. However, we could not find such pixels, indicating that our A_V map is not heavily affected by YSOs.

Finally, in order to evaluate the possible error due to the intrinsically red sources, we actually reproduced an A_V map excluding the sources on the right side of the broken line, which we then compared to our original map in Fig. 5, where YSOs and AGBs are not excluded. The two maps agree fairly well in the low A_V range (≤ 2 mag), although the original map shows higher A_V values by a factor of ~ 2 at most in the higher A_V range (> 2 mag). The difference is likely due to having removed the reddened field stars in the process, because we could not identify apparent clusters of YSOs in regions with the highest A_V values. Furthermore, we note that we applied the correlation analysis described in Sect. 3 to both maps. We found that the results given in Sect. 3 are in good agreement within the error for both of maps.

2.4. Relative distribution of clouds and stars

As demonstrated in Fig. 2, plots of E_{X_0} and E_{X_m} as a function of X_0 contain information about the respective geometry of the clouds and stars in the LMC. The shape of the plot depends on the cloud position Z and the cloud thickness T . We compared the observed E_{X_0} and E_{X_m} with the model calculations, in order to measure the location of the clouds along the line of sight in the LMC. This comparison should also give us an estimate of the true color excess of the clouds, E_0 .

We illustrate our model comparison method for cloud LMC-154 in Fig. 8. The model parameters are the cloud position Z , the cloud thickness T , the background color excess E_{bg} , the color excess due to the cloud E_0 , the percentiles of star colors X_0 and X_1 , and the intrinsic dispersion of star colors σ (see Fig. 1). We allowed Z , T , and E_0 to be free parameters in the model calculations, and fixed the remaining parameters. X_1 was set to 95% as we measured the color excess using Eqs. (1) and (2) at this percentile. The value of E_{bg} was assumed to be 0.25 mag for the color $J - H$, and 0.20 mag for $H - K_S$. The assumed values for E_{bg} are based on the background

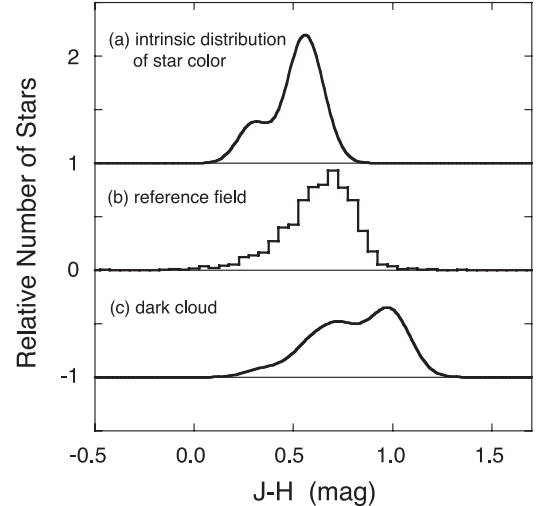


Fig. 9. Distributions of star color $J - H$ around the cloud LMC-154. **a)** Inferred intrinsic color distribution derived from the observed color distribution in the reference field assuming the background $E_{bg} = 0.25$ mag. **b)** Observed color distribution in the reference field measured using stars within $10'$ around the position $\alpha_{2000} = 5\text{h}28\text{m}46.5\text{s}$ and $\delta_{2000} = -68^\circ 13' 23''$. **c)** Inferred color distribution reddened by the cloud with the color excess $E_0 = 0.25$ mag. The color distributions in panels **a)** and **c)** are calculated from the observed distribution in panel **b)** using the model shown in Fig. 1 with parameters $[T, Z] = [40, 10]\%$ and $[E_{bg}, E_0] = [0.25, 0.25]$ mag. The three color distributions shown in this figure correspond to those in Fig. 1.

HI intensity around LMC-154. We applied a $1^\circ \times 1^\circ$ median filter to the HI map obtained by Kim et al. (2003), and found that the intensity of the resulting HI map corresponds to an HI column density of $\sim 1.0 \times 10^{22}$ H cm^{-2} , which we regard as the background hydrogen column density around the cloud. If we assume that the ratio $\frac{A_V}{N_{\text{H}}}$ is roughly one half of the galactic value (5.34×10^{-22} mag/ H cm^{-2} , Bohlin et al. 1978, assuming $R_V = 3.1$) and that the relations given in Eqs. (6) and (7) are valid, the background column density provides an estimate of the E_{bg} values. The intrinsic dispersion of the star colors was estimated from the actual star color distribution observed in the reference field close to LMC-154. We inferred the intrinsic distribution of star colors assuming that the stars observed in the reference field are reddened by E_{bg} stated above. In Fig. 9, we show the distribution of $J - H$ observed in the reference field and the intrinsic color distribution inferred for the background $E_{bg} = 0.25$ mag. We also show the color distribution inferred at the centre position of LMC-154 for the color excess $E_0 \sim 0.25$ mag in $J - H$.

Using the parameters described above, we performed model calculations as described in Sect. 2.1 to determine the set of the parameters $[E_0, Z, T]$ that minimize χ^2 for the observed E_{X_0} vs. X_0 and E_{X_m} vs. X_0 diagrams at the positions labelled “A”–“D” in LMC-154 shown in Fig. 8. Results for the $J - H$ color are shown in Fig. 10. A rather large mismatch between the model and the observed data is evident at position A for $X_0 \geq 85\%$. This might be due to contamination by YSOs with extremely red colors (see Sect. 2.3). Furthermore, some data points give negative values for the color excess at low X_0 values for positions A, C, and D, which is an artifact caused by the median filter that we applied to subtract the background. In other respects, the results of the model calculations trace the overall distributions of the data points, indicating that our simple model

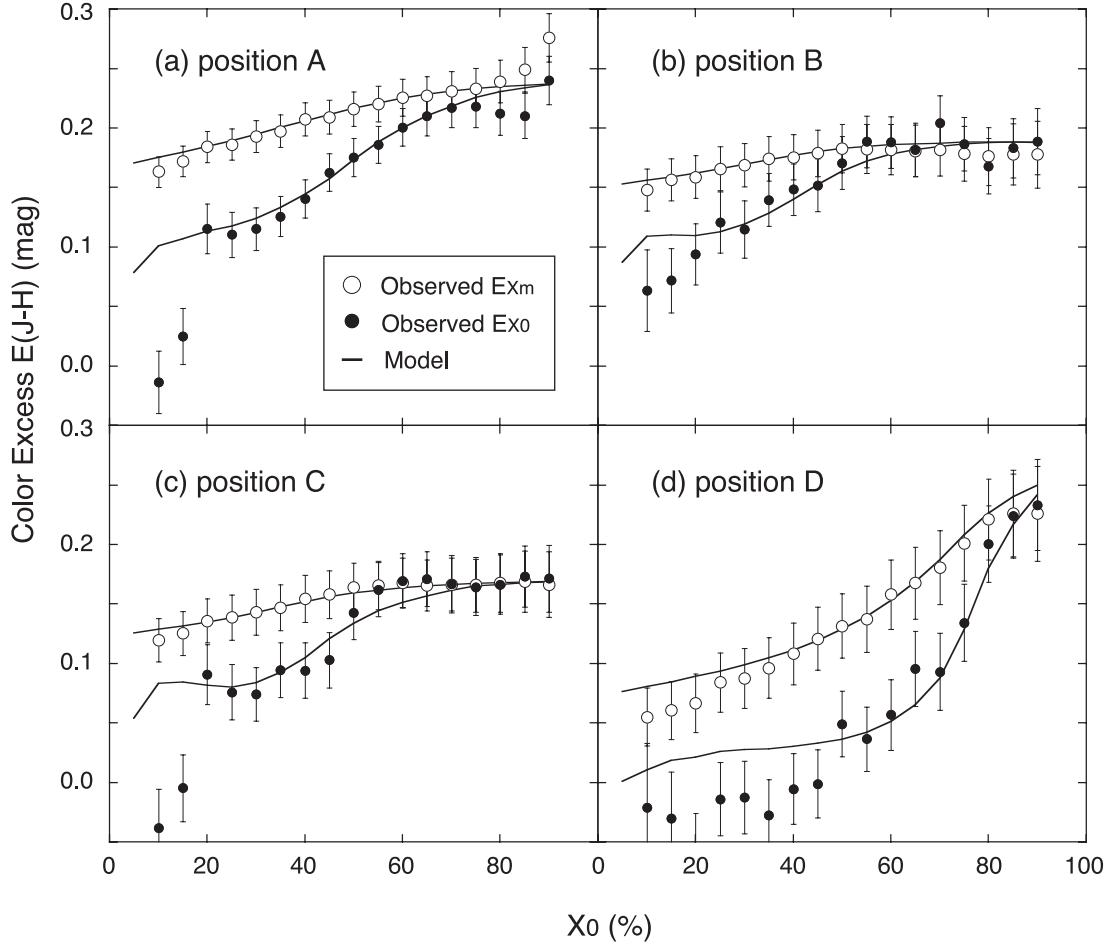


Fig. 10. Sample of E_{X_0} (filled circles) and E_{X_m} (open circles) measured as a function of X_0 around the cloud LMC-154 (X_1 is fixed to 95%). Data shown in panels a)–d) are sampled by averaging some pixels around the positions labelled “A”–“D” in Fig. 8. Solid lines denote the best-fitting model values with parameters $[E_0, T, Z] = [0.24 \text{ mag}, 40\%, 10\%]$, $[0.19 \text{ mag}, 15\%, 15\%]$, $[0.17 \text{ mag}, 5\%, 25\%]$, and $[0.28 \text{ mag}, 10\%, 65\%]$ for the data shown in the panels from a) to d) in this order. In the model calculation to derive the best-fitting values, we used the intrinsic star color distribution shown in Fig. 9a inferred for a background extinction of $E_{\text{bg}} = 0.25 \text{ mag}$.

works well for this cloud. We note that the difference between the best fitting E_0 value and the observed color excess is small for high X_0 values, especially when the curves of the E_{X_0} and E_{X_m} are convex upward (i.e., $\frac{d^2 E}{dX_0^2} < 0$), while the difference is larger if the curves are concave. For instance, at $X_0 = 80\%$, the difference is only $\lesssim 5\%$ at positions A, B, and C, but it can be up to $\sim 20\%$ at the position D. Convex curves are generally seen for clouds with the sum of the cloud parameters $Z + T \lesssim 50\%$, while concave curves are typical of clouds with $Z + T > 50\%$. Note that the sum of the parameters $Z + T$ defines the position of the far-side of the cloud. It thus appears that cloud LMC-154 is located mostly in front of the star population along the line of sight, except for a region around position D. Our estimate of the cloud position agrees with the fact that the cloud is seen as an obscured region in optical images (such as DSS), independent evidence that the majority of stars along the line of sight of the cloud lie in the background. It is also notable that the velocity of the CO emission around the position D ($V_{\text{LSR}} \sim 253 \text{ km s}^{-1}$, Fukui et al. 2008) differs from the velocities measured for other parts of LMC-154 ($\sim 255\text{--}261 \text{ km s}^{-1}$), supporting our idea that the dark cloud near position D is located at a different position, probably towards the back of the LMC compared to other parts of the cloud.

In order to measure the location of clouds in the LMC along the line of sight, we applied the fitting procedure described above to the entire region shown in Fig. 5. The background reddening E_{bg} and the intrinsic star color distribution should vary from region to region in the LMC, but for simplicity we assumed the same background and color distribution as those for the cloud LMC-154. Resulting maps of the best-fitting color excess (E_0 in $J - H$) and cloud positions (Z and $Z + T$) are shown in Fig. 11. There are some regions in this figure that exhibit very high $Z + T$ values, for example around the positions ($\alpha_{2000} = 5^{\text{h}}40^{\text{m}}$, $\delta_{2000} = -69^{\circ}20'$) and ($\alpha_{2000} = 5^{\text{h}}35^{\text{m}}$, $\delta_{2000} = -67^{\circ}0'$). These regions correspond to the positions of OB associations in the LMC, and the artificially high $Z + T$ values are due to the much bluer star colors than the intrinsic star colors that we assumed. Except for such regions, the Z and $Z + T$ maps provide a rough picture of the relative distribution of the clouds and stars along the line of sight. For instance, LMC-114 in the vicinity of LMC-154 appears to be located behind LMC-154. It is interesting to note that there is a clear difference in the velocity of the CO emission from these two clouds ($V_{\text{LSR}} \sim 280 \text{ km s}^{-1}$ for LMC-114, and $\sim 255\text{--}260 \text{ km s}^{-1}$ for LMC-154), also suggesting that they are in different locations in the LMC. The locations of clouds within the 30 Dor region are complex and erroneous due to the large number of OB stars, but clouds in the

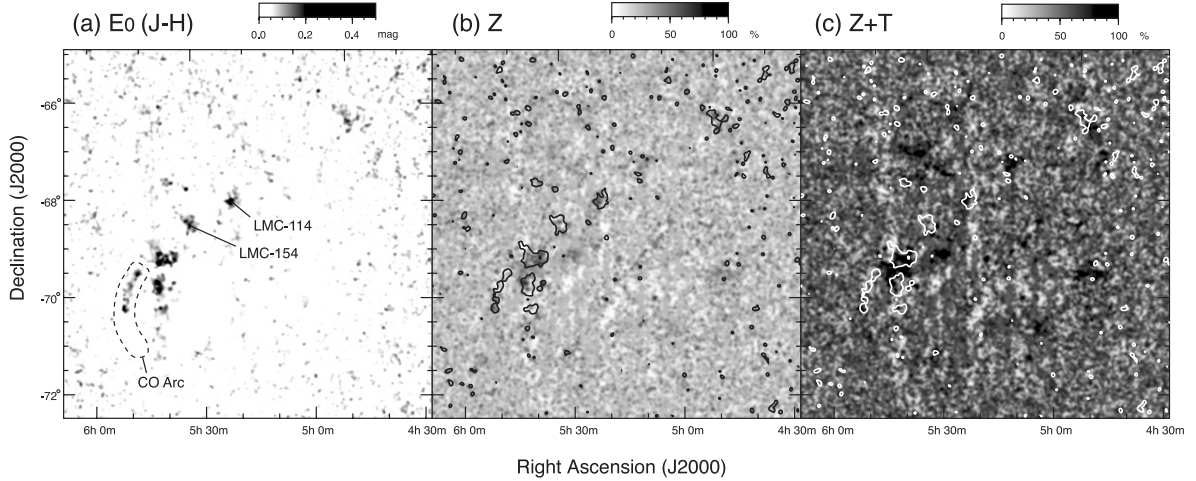


Fig. 11. Distribution of model parameters that best fit the observed color excess $E(J-H)$: **a)** color excess due to dark clouds E_0 , **b)** position of the near side of the clouds Z , and **c)** position of the far side of the clouds ($Z+T$). For comparison, locations of the clouds are indicated in the panels **b)** and **c)** by black and white contours at $E_0 = 0.09$ mag, respectively.

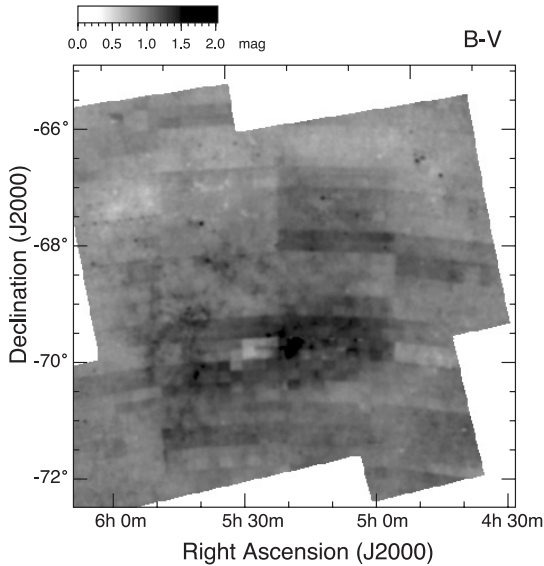


Fig. 12. Distribution of the star color $B-V$ produced using a part of the star catalog compiled by Zaritsky et al. (2004). The map displays the mean color calculated based on Eq. (2) for $[X_0, X_1] = [80, 90]\%$. The angular resolution of the map is the same as in Fig. 5 (2'6).

region around the position $\alpha_{2000} = 5^{\text{h}}42^{\text{m}}$ and $\delta_{2000} = -70^{\circ}20'$ are apparently located towards the front of the LMC. Clouds in the CO arc are well-detected in CO (Mizuno et al. 2001; Fukui et al. 2008), but they are only apparent in the northern half of the arc in our extinction map. This may be because the clouds in the southern half of the arc are closer to the far side of the LMC (Fig. 11c), making it difficult to detect them in extinction even using our new method. Although the maps for the best fitting parameters E_0 , Z , and $Z+T$ shown in Fig. 11 are still rather noisy, we note that this technique to probe the location of clouds along the line of sight would work better if the variation of the intrinsic star color distribution and the background color excess were better determined.

2.5. Comparison with the optical data

We compare the extinction map derived from 2MASS in this paper with the optical data obtained by Zaritsky et al. (2004). These

authors presented a catalog of more than 2.4×10^7 stars in the central 64 deg^2 area of the LMC, providing U , V , B , and I band photometry of the stars. They also attempted to estimate the line-of-sight visual extinction (A_V) toward the individual stars based on stellar atmosphere models. Their catalog is extensive and moderately deep – complete in detection down to ~ 20 mag in V band – although the photometric uncertainties are somewhat large.

In order to investigate the color excess $E(B-V)$ due to dark clouds in the LMC, we selected stars brighter than 19 mag in both B and V bands in the Zaritsky et al. (2004) catalog, and processed the data in the same manner as we did for the 2MASS data. In Fig. 12, we show the resulting $B-V$ map, i.e., C_{X_m} in Eq. (2) at $[X_0, X_1] = [80, 95]\%$. Although the $B-V$ map suffers from a systematic error in photometry apparently due to the drift-scans, the map traces the extinction regions similar to those revealed in the 2MASS-based A_V map (Fig. 5). We further processed the mean star color map in Fig. 12 to derive the color excess map $E(B-V)$. Figure 13a shows a part of the color excess map around the cloud LMC-154, corresponding to E_{X_m} in Eq. (4) at $[X_0, X_1] = [80, 95]\%$.

In addition to the color excess $E(B-V)$, we obtained an estimate of the total extinction toward the individual stars around LMC-154 using the program “Reddening Estimator” that was described in Zaritsky et al. (2004) and is available on the internet (URL <http://ngala.as.arizona.edu/dennis/lmcext.html>). Using both “hot” and “cool” stars in their catalog, we reduced the extinction data of the stars in the same manner as for the other maps, finding the X percentile extinct stars in each cell to derive an A_V map for the range $[X_0, X_1] = [80, 95]\%$. We display the resulting extinction map in Fig. 13b, and henceforth refer to it as “the A_V^Z map”.

Overall, the shapes of the dark clouds in the 2MASS-derived A_V , $E(B-V)$, and A_V^Z maps are similar, but there are some significant differences (cf., Figs. 8, 13a, and b). The cloud contrast is clearly different in the three maps in the north-eastern and the central parts of LMC-154, although the results are more similar for the southern parts of the cloud. This may be due to the difference in the optical depth of the 2MASS and the catalog of Zaritsky et al. (2004), resulting in a difference of the regions along the line of sight traced by the maps. In addition, the optically thinner 2MASS-based A_V map might be contaminated by

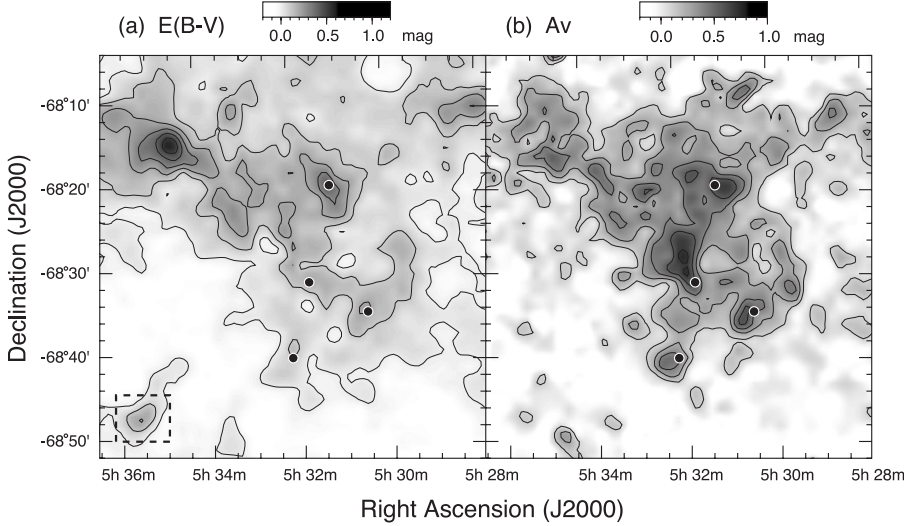


Fig. 13. Maps of **a)** the color excess $E(B - V)$ and **b)** the visual extinction of A_V (i.e., A_V^Z in text) around LMC-154 derived from the star catalog of Zaritsky et al. (2004). Both maps were derived in the same way as the A_V map shown in Fig. 8 derived using the 2MASS catalog. The A_V map in panel **b)** was derived on the basis of the total extinction toward the individual stars calculated by the “Reddening Estimator” developed by Zaritsky et al. (2004) (see text). In panel **a)**, the contours indicate increments of $\Delta E(B - V) = 0.1$ mag, starting from $E(B - V) = 0$ mag. In panel **b)**, the contours represent increments of $A_V = 0.15$ mag and start from $A_V = 0.1$ mag. Dots indicating the positions “A”–“D” in Fig. 8 are shown for comparison. The box drawn with broken lines in the lower-left corner in panel **a)** marks the region where the data shown in Fig. 14 are sampled.

YSOs in the central part of the cloud (cf., around the position “A” in Fig. 8), although they are expected to be ruled out from our star sample (Sect. 2.3).

For a small region indicated by the broken lines in the bottom-left corner of Fig. 13a, we attempted to measure the visual extinction by the traditional star count method using the V band data taken from the catalog of Zaritsky et al. (2004). We measured the star density distribution N in the small region using stars in the catalog with a V band magnitude $m_V \leq 19$ mag. We then generated the Wolf diagram around the small region, i.e., the m_V vs. $\log(N)$ relation, to measure its slope b . These quantities yield an estimate of the visual extinction A_V as,

$$A_V = \frac{1}{b}(\log N_0 - \log N), \quad (10)$$

where N_0 is the background star density. We found the slope of the Wolf diagram to be $b = 0.5$ at $m_V = 19$ mag. The background stellar density N_0 varies significantly over the LMC, but we considered it to be constant in the small region. However, the absolute value of N_0 for the small region is still difficult to determine precisely, and we therefore adopted the average stellar density around the small region as N_0 . Error in our determination of N_0 will result in an offset in A_V derived using Eq. (10). Henceforth, we denote the visual extinction measured by the star count method as A_V^{sc} .

In Fig. 14a, we show the relations between $E(B - V)$ and A_V^Z , A_V^{sc} , and 2MASS-derived A_V . We determined the best linear least-squares fit to the plots of the extinction estimates as a function of $E(B - V)$. Although all three extinction estimates and $E(B - V)$ will contain an offset due to the unknown background extinction and the median filter that we applied, it is important to note that the slopes of the fitted lines should trace their relationship, regardless of these offsets. Note also that the slopes correspond to the ratio of total to selective extinction, R_V , relating A_V and $E(B - V)$ as $A_V = R_V E(B - V)$.

As seen Fig. 14a, R_V is found to be 3.2 for A_V^{sc} , which is consistent with our assumption for R_{λ_1, λ_2} in Eq. (5). However, the resulting 2MASS-derived A_V values are ~ 2.7 times higher than A_V^{sc} , corresponding to a high R_V of 8.6. In order to confirm this discrepancy, we plot the relationship between $E(B - V)$ and $E(J - H)$, shown in Fig. 14b. Note that the slope of the best fitting line for the data in this plot corresponds to the ratio $\frac{R_V}{R_{JH}}$, where R_{JH} is the coefficient in Eq. (6). If we assume the reddening law

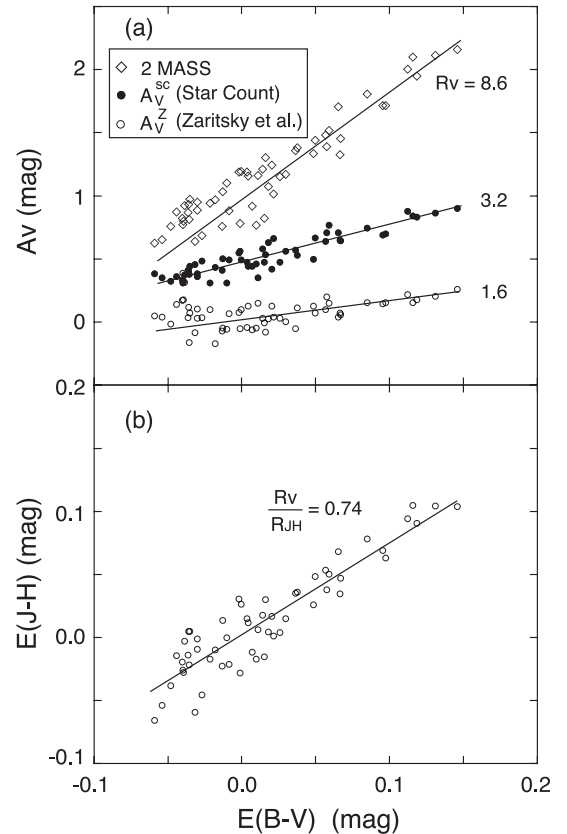


Fig. 14. **a)** Correlations between $E(B - V)$ shown in Fig. 13a and A_V derived in the three different ways measured towards a small cloud in the vicinity of LMC-154. Diamonds denote the 2MASS-based A_V values derived in this paper (Fig. 8), and filled circles indicate the extinction A_V^{sc} measured using star counts in V band. Open circles denote the extinction A_V^Z derived using the program “Reddening Estimator” prepared by Zaritsky et al. (2004) and available online (Fig. 13b, see text). The vertical axis is offset by $A_V = 1.2$ mag and 0.5 mag for the 2MASS-based A_V and A_V^{sc} respectively. **b)** Correlation between $E(J - H)$ and $E(B - V)$ measured from 2MASS and the catalog of Zaritsky et al. respectively. In both panels, the linear relations that best fit the data are shown by the solid lines. Note that the slopes of the lines in the panels **a)** and **b)** are equivalent to R_V and R_V/R_{JH} respectively. All of the plotted data are taken in the region denoted by the box drawn with broken lines in Fig. 13a.

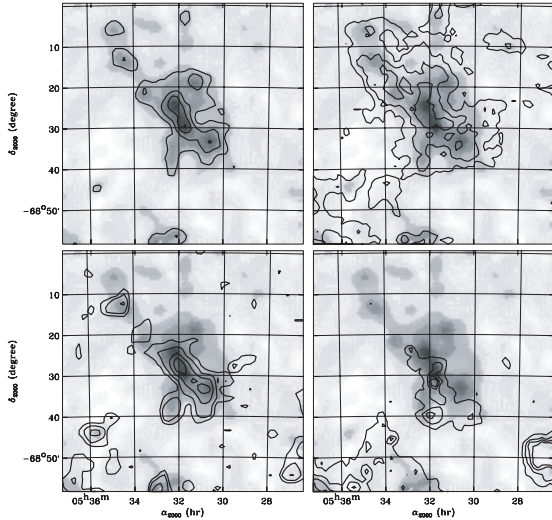


Fig. 15. Extinction map around the cloud LMC-154. The image shows the extinction map derived from star colors in the 2MASS catalog. The gray scale ranges from -0.5 (white) to 2.5 mag (black). The various panels show contours for the extinction (*upper-left*) with contours at 0.5 , 1.0 , 1.5 and 2.0 mag, H I integrated intensity (*upper-right*) with contours at 0.7 , 1.0 and 1.3×10^4 K km s $^{-1}$, CO integrated intensity (*lower-left*) with contours at 0.5 , 1 , 2 , 3 , 4 , 6 , 8 and 10 K km s $^{-1}$, and H α emission (*lower-right*) with contours at 1 , 2 , 3 and 4×10^2 R (Rayleighs).

of Cardelli et al., the ratio $\frac{R_V}{R_{JH}}$ should be ~ 0.28 for $R_V = 3.1$, while we find $\frac{R_V}{R_{JH}} = 0.74$. A high R_V value of ~ 7 is required to reproduce the observed $\frac{R_V}{R_{JH}}$ ratio, indicating the same discrepancy that was observed in Fig. 14a.

To summarize, the optical data $E(B - V)$ and A_V^{sc} are consistent with our assumption of $R_V \sim 3$, while the 2MASS-derived A_V , based on the reddening law of Cardelli et al. (1989), is ~ 3 times higher than A_V^{sc} . This implies that the reddening law of Cardelli et al. may not be valid in the LMC at near infrared wavelengths, and that we may be overestimating the visual extinction by a factor of ~ 3 . However, we shall continue to use the assumption of the reddening law of Cardelli et al. in this paper, because it is known that star counts tends to underestimate the true extinction, especially when clouds are contaminated by foreground stars, and also because the uncertainties in the optical photometry from Zaritsky et al. (2004) might be too large to measure $E(B - V)$ precisely. In particular, we note that A_V^Z is lower than A_V^{sc} by a factor of 2 (Fig. 14a). Since the star count method will tend to underestimate the true visual extinction, A_V^{sc} should provide a lower limit to the actual A_V . A_V^Z is therefore also likely to be an underestimate of the true extinction. The coefficients in Eqs. (6) and (7) should be rescaled when the relations between A_V , $E(J - H)$, and $E(H - K_S)$ in the LMC are better established.

3. A_V vs. N_H correlations

As demonstrated in Fig. 15, our A_V map is apparently correlated well with the gas emission in the LMC. In this section, we perform a correlation analysis of their relation.

Dust extinction at visible and near-infrared wavelengths is produced by large dust grains (Big Grains, BGs), while extinction in the UV and FUV is caused by smaller particles. The BGs dominate the total dust mass of a galaxy. In principle, the spatial distribution of dust extinction derived from IR measurements

can be compared to the gas distribution, in order to derive the dust abundance and its spatial variation. Furthermore, if the optical properties of dust grains in the molecular phase of the ISM are known, extinction maps can also be used to infer the elusive conversion factor between the intensity of the CO line emission and the column density of H $_2$, X_{CO} . Since the metallicity of the LMC is known to be significantly lower than in our Galaxy, we might expect that the appropriate value of X_{CO} will also differ, due to the lower abundance of dust and heavy elements that contribute to the production of CO molecules.

For clouds in the solar neighborhood, there is some evidence that the abundance of the smallest dust particles is highly variable. Polycyclic Aromatic Hydrocarbons (PAHs), which can be considered as the smallest dust particles, show large abundance variations from cloud to cloud (e.g., Boulanger et al. 1990; Miville-Deschênes et al. 2002), and from the inner depths of translucent clouds to their peripheral haloes (e.g., Bernard et al. 1993). These variations sometimes involve a significant overabundance of PAHs with respect to their abundance in the diffuse ISM, suggesting that PAHs may be formed locally in these regions, perhaps via the erosion of larger carbonaceous grains. Intermediate-sized grains (Very Small Grains, VSGs) also show evidence for significant variations in their size distribution in the LMC (e.g., Sakon et al. 2006; Bernard et al. 2008). In the Milky Way, abundance variations of the VSGs have been observed in some clouds using IRAS data (e.g., Laureijs et al. 1991). These data reveal a tendency for lower VSG abundances in some dense molecular regions, such as the Taurus complex (Abergel et al. 1994). These variations have been interpreted as evidence for adhesion of VSGs onto the surface of big grains in quiescent environments with sufficient density (Bernard et al. 1999; Stepnik et al. 2003). This coagulation process appears to be simultaneous with mutual coagulation of the large grains into fractal aggregates, which has been observed indirectly through a drop in the equilibrium temperature of the BGs.

It can therefore be concluded that small grains are unlikely to trace the total column density accurately at small scales in the ISM. Large grains, however, are expected to be more stable. Indeed, there is no clear evidence that the BG abundance relative to gas varies significantly in the MW, independent of large scale variations that may be due to metallicity gradients. A comparison between the abundance of large grains in the MW and the Magellanic Clouds shows a systematic decrease of the BG abundance with metallicity, as expected (see Bernard et al. 2008; Bot et al. 2004). While the BG abundance could vary on large scales within galaxies if large metallicity gradients are present, no significant variations are expected on the size scales of giant molecular clouds.

In principle, changes to the large grain size distribution, either through grain growth or grain aggregation, could lead to changes in the optical properties of BGs. At submillimeter wavelengths, this process has been invoked to produce an increase of the dust emissivity by a factor of a few, which is necessary to explain the cold dust temperature observed towards some clouds (Bernard et al. 1999; Stepnik et al. 2003). The effect of dust coagulation on the optical dust properties has been evaluated by several authors. Detailed calculations by Ossenkopf (1993) indicate a clear increase of the optical depth by a factor of a few in the FIR and submillimeter regime, consistent with the observations of Stepnik et al. (2003). The increase in optical depth at NIR wavelengths is much smaller, however, especially when ice mantles covering the grains are taken into account. Grain growth has also been advocated to explain the observed changes of the total to selective absorption ratio R_V in dense regions (e.g.,

Kandori et al. 2003). However, the empirical law of Cardelli et al. (1989) indicates that the shape of the extinction curve is mostly independent of R_V below $\lambda = 0.7 \mu\text{m}$.

It is therefore legitimate to assume that at the NIR wavelengths at which we have derived our extinction maps, the optical properties of dust dominating the extinction are independent of the ISM phase. For the following analysis, we assume a constant ratio of extinction to hydrogen column density in the neutral and molecular gas phases.

3.1. Gas tracers

To trace the atomic gas in the LMC, we use the HI 21-cm line map from Kim et al. (2003), which combines data from the Australia Telescope Compact Array (ATCA) and the single-dish Parkes Telescope. The field-of-view of the combined data is $11.1^\circ \times 12.4^\circ$. The angular resolution of the data is $1'$, corresponding to a physical resolution of ~ 14.5 pc at the distance of the LMC. The useful heliocentric velocity coverage is from -33 to 627 km s^{-1} , with a velocity resolution of 1.649 km s^{-1} . The rms noise level in the final spectral line cube is 2.5 K.

To trace the molecular gas, we use the ^{12}CO ($J = 1-0$) line map obtained using the NANTEN telescope, a 4 m radio telescope of Nagoya University situated at Las Campanas Observatory in Chile (see Fukui et al. 2008). The observed region covers about 30 square degrees where CO clouds were detected in the first NANTEN survey of ^{12}CO ($J = 1-0$) emission in the LMC (Mizuno et al. 2001). In total, about 26 900 positions were observed in equatorial coordinate position switching mode. The grid spacing of the observations was $2'$, corresponding to about 30 pc at the distance of the LMC, while the half-power beam width (HPBW) of the telescope is 2.6 at 115 GHz. The integration for each ON-position in the survey was about three minutes. The rms noise fluctuations in the final cube are about 0.07 K at a velocity resolution of 0.65 km s^{-1} . The typical 3-sigma noise level of the velocity-integrated intensity map is 1.2 K km s^{-1} .

Assuming that the molecular clouds detected in the NANTEN survey are in gravitational equilibrium, it is possible to derive a value of the CO-to- H_2 conversion factor, X_{CO} . A preliminary analysis of the data indicated an average value of $X_{\text{CO}} = 9 \times 10^{20}$ $\text{H}_2 \text{ cm}^{-2}/(\text{K km s}^{-1})$ across the LMC (Mizuno et al. 2001). More recently, Fukui et al. (2008) analyzed the second NANTEN survey of the ^{12}CO ($J = 1-0$) emission in the LMC and derived an average value of $X_{\text{CO}} = 7 \times 10^{20}$ $\text{H}_2 \text{ cm}^{-2}/(\text{K km s}^{-1})$, using an improved method for identifying the cloud surfaces and extrapolating the CO emission profiles down to the noise level. For our analysis, we adopt $X_{\text{CO}} = 7 \times 10^{20}$ $\text{H}_2 \text{ cm}^{-2}/(\text{K km s}^{-1})$ as the average CO-to- H_2 conversion factor for the LMC, and use the cloud properties measured by Fukui et al. (2008) for each cloud in the survey.

The total mass of molecular gas in the LMC is about $5 \times 10^7 M_\odot$. The distribution of the CO emission in the LMC is clumpy, with several massive molecular cloud complexes, quite unlike the filamentary and shell-like structures observed for the HI gas distribution. Fukui et al. (2008) identify 272 molecular clouds in the LMC, about a 1/4 of which are associated with optically-identified young clusters (type III clouds). Approximately half the molecular clouds are associated with optically-identified H II regions (type II), while the remaining clouds (type I) are not associated with any optical indicator of massive star formation.

3.2. Correlation results

The total visible extinction is due to dust located in the atomic and molecular phases as follows:

$$A_V = \alpha W_{\text{HI}} + \beta W_{\text{CO}} + A_V^0, \quad (11)$$

where α and β are free parameters, W_{HI} and W_{CO} are the HI and CO line integrated intensities respectively, and A_V^0 is a residual extinction. The HI and CO maps entering Eq. (11) have been filtered in the same way as the A_V data (see Sect. 2), subtracting from the original map a median filtered version of the map, with a kernel size of 1° .

To account for Galactic extinction towards the LMC, we used a map of the foreground HI column density constructed by Staveley-Smith (2003) by integrating the Parkes HI data in the heliocentric velocity range -64 km s^{-1} to 100 km s^{-1} . This range excludes gas associated with the LMC ($v > 100$ km s^{-1}), but includes most of the local Galactic emission. The Galactic HI column density is as much as $N_{\text{H}} = 1.3 \times 10^{21}$ H cm^{-2} , with significant variations, across the LMC. The foreground HI map was projected onto the extinction maps derived in Sect. 2 and the corresponding extinction was estimated assuming $\frac{A_V}{N_{\text{H}}} = 5.34 \times 10^{-22}$ $\text{mag}/(\text{H cm}^{-2})$. The average MW extinction across the LMC was found to be $A_V \simeq 0.2$ mag. The map of extinction due to the foreground Galactic HI column density was median-filtered in the same way as the LMC extinction map and subtracted from the LMC extinction map derived in Sect. 2.

The free parameters α and β in Eq. (11) can be expressed as

$$\alpha = \left(\frac{A_V}{N_{\text{H}}}_{\text{HI}} \right) X_{\text{HI}} \quad (12)$$

$$\beta = 2 \left(\frac{A_V}{N_{\text{H}}}_{\text{CO}} \right) X_{\text{CO}}, \quad (13)$$

where $\left(\frac{A_V}{N_{\text{H}}}_{\text{HI}} \right)$ and $\left(\frac{A_V}{N_{\text{H}}}_{\text{CO}} \right)$ are the extinction to total column density ratio in the atomic and molecular phases respectively, X_{HI} is the conversion factor from W_{HI} to N_{H} (assumed to be $X_{\text{HI}} = 1.82 \times 10^{18}$ $\text{H cm}^{-2}/(\text{K km s}^{-1})$), and X_{CO} is the conversion factor from W_{CO} to the column density of H_2 .

Assuming the dust associated with atomic and molecular gas has the same abundance and optical properties,

$$\left(\frac{A_V}{N_{\text{H}}}_{\text{HI}} \right) = \left(\frac{A_V}{N_{\text{H}}}_{\text{CO}} \right) = \frac{A_V}{N_{\text{H}}}, \quad (14)$$

the $\frac{A_V}{N_{\text{H}}}$ and X_{CO} factor can be derived from the fitted parameters using

$$\frac{A_V}{N_{\text{H}}} = \frac{\alpha}{X_{\text{HI}}} \quad (15)$$

$$X_{\text{CO}} = \frac{\beta X_{\text{HI}}}{2\alpha}. \quad (16)$$

Note that the measurements actually only constrain the product of $\frac{A_V}{N_{\text{H}}}$ and X_{CO} , as shown in Eq. (13). If the absorptivity of the ISM is overestimated, the derived X_{CO} factor will be correspondingly underestimated. The estimate for X_{CO} in Eq. (16) should therefore be considered as a local conversion factor. Since we attempt to separate the contribution of the two phases from the correlation, our X_{CO} estimate represents the ratio between the H_2 column density associated with the CO-emitting gas and the integrated CO emission of the same CO-emitting volume of gas. It does not necessarily trace the ratio of the total H_2 column density to CO emission along a given line of sight, particularly if the

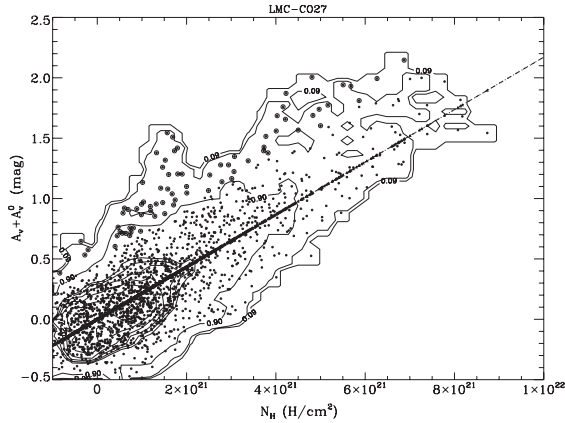


Fig. 16. Correlation between A_V and N_H in LMC-154. Contours indicate the density of data points. The dashed line shows the best-fitting model. Encircled symbols show points with an A_V excess above 0.5 mag.

H_2 and CO are not co-located. This is an important caveat that will be discussed further in Sect. 4.

For each region, we derive the two free parameters (α and β) in Eq. (11) using the IDL routine `regress`, and derive errors on these parameters using the formal errors on A_V and on the HI and CO integrated intensities. In practice, we first subtract a constant from the HI, CO and A_V map before performing the linear regression. The region of the maps used to derive this constant value is selected in the lowest 50% percentile of the HI map where $W_{CO} \leq 0.1 \text{ K km s}^{-1}$.

Errors on $\frac{A_V}{N_H}$ and X_{CO} are computed as

$$\Delta \frac{A_V}{N_H} = \frac{\Delta \alpha}{X_{HI}} \quad (17)$$

$$\Delta X_{CO} = \frac{X_{HI}}{2} \left(\frac{\Delta \alpha}{\alpha} + \frac{\Delta \beta}{\beta} \right), \quad (18)$$

where $\Delta \alpha$ and $\Delta \beta$ are the formal regression errors on the free parameters α and β , given the errors on W_{HI} , W_{CO} , and A_V . Figure 16 illustrates the correlation between the measured extinction and the total gas column density around one of the clouds in our sample. The gas column density is computed using

$$N_H = N_H^{HI} + N_H^{CO} = X_{HI} W_{HI} + 2 X_{CO} W_{CO}. \quad (19)$$

The straight line shown in Fig. 16 is the correlation given by Eq. (11). The black contours indicate the density of points.

3.3. Global results

Initially, we performed the correlation analysis described in Sect. 3.2 over the whole extent of the LMC. The corresponding values derived are given in Table 2 under the region name “AllLMC”. The derived absorptivity is $\frac{A_V}{N_H} = 1.7 \times 10^{-22} \text{ mag}/(\text{H cm}^{-2})$, about three times lower than the adopted reference value in the solar neighborhood ($5.34 \times 10^{-22} \text{ mag}/(\text{H cm}^{-2})$). The average value derived for the X_{CO} factor is $X_{CO} = 2.26 \times 10^{20} \text{ H}_2 \text{ cm}^{-2}/(\text{K km s}^{-1})$. This is about 1.2 times higher than the standard value adopted for the Milky Way ($1.8 \times 10^{20} \text{ H}_2 \text{ cm}^{-2}/(\text{K km s}^{-1})$, Strong & Mattox 1996), and about three times lower than the average value in the LMC ($X_{CO} = 7 \times 10^{20} \text{ H}_2 \text{ cm}^{-2}/(\text{K km s}^{-1})$) derived from a virial analysis of the NANTEN CO data (Fukui et al. 2008).

Next, we conducted the correlation analysis using a set of annuli of increasing radius centred on the 30 Dor region ($d_{30 \text{ Dor}}$).

The derived values of $\frac{A_V}{N_H}$ and X_{CO} are shown by the solid lines in Fig. 17. It can be seen that $\frac{A_V}{N_H}$ decreases systematically from $\frac{A_V}{N_H} \approx 2.5 \times 10^{-22} \text{ mag}/(\text{H cm}^{-2})$ close to 30 Dor, down to $\frac{A_V}{N_H} = 0.63 \times 10^{-22} \text{ mag}/(\text{H cm}^{-2})$ in the outskirts of the LMC. A similar trend was reported by Bernard et al. (2008) for the FIR emissivity, with τ^{160}/N_H rising from the outer regions of the LMC (where $\tau^{160}/N_H \approx 8.8 \times 10^{-26} \text{ cm}^2$) towards two molecular clouds located about 1° from 30 Dor (where $\tau^{160}/N_H \approx 2.5 \times 10^{-25} \text{ cm}^2$ in the neutral phase surrounding the clouds). Both the apparent emissivity and absorptivity of the dust thus seem to decrease significantly with increasing distance from 30 Dor, although the amplitude of the spatial variations seems larger in absorption (a factor of ~ 4) than in emission (a factor of less than 2.8). The radial profile obtained for X_{CO} is reasonably flat in the inner 3° surrounding 30 Dor. Towards the outer regions of the LMC, the CO emission is very low and the X_{CO} estimates become very noisy. For clarity, the X_{CO} estimates at large radii from 30 Dor are not shown in Fig. 17.

3.4. Results for individual clouds

We selected individual regions to be studied in more detail by visually inspecting the A_V and CO maps. These regions are indicated in Fig. 18. We selected regions with significant extinction over several contiguous pixels in the extinction map, and with significant CO emission over a similar area. The selected regions include massive CO complexes with strong evidence of active star formation, mostly located around the 30 Dor region, as well as more quiescent clouds. The regions should therefore be representative of the molecular emission across the LMC. Each region typically includes several individual CO clouds as defined by Fukui et al. (2008). The average cloud properties within each region are given in Table 1. We list L_{CO} -weighted average values, where values for individual clouds have been taken from Fukui et al. (2008). As noted in Sect. 2.4, some regions in the LMC have CO emission with no detectable extinction, which is likely to be due to the molecular cloud’s unfavorable location compared to the stellar distribution along the line of sight. Such regions were not included in the sample selected for our correlation analysis.

Table 2 lists our derived $\frac{A_V}{N_H}$ and X_{CO} , their 1σ errors and the reduced χ^2 of the linear regression. For all regions, it can be seen that the quality of the regression is satisfactory within the errors. Our derived $\frac{A_V}{N_H}$ values vary from 0.4 to $3.7 \times 10^{-22} \text{ mag}/(\text{H cm}^{-2})$, similar to the range determined from a global analysis, with an ensemble average of $1.9 \times 10^{-22} \text{ mag}/(\text{H cm}^{-2})$, using a weight inversely proportional to the square of the errors. The average value is once again lower than the Galactic value of $\frac{A_V}{N_H}$ by a factor of ~ 3.6 .

Figure 17 suggests that the $\frac{A_V}{N_H}$ values for individual regions may follow the same trend as the values derived using the set of annuli centred on 30 Dor. Regions located within $\approx 1^\circ$ of 30 Dor have an average $\frac{A_V}{N_H} \approx 2.8 \times 10^{-22} \text{ mag}/(\text{H cm}^{-2})$, while those further away have an average $\frac{A_V}{N_H} \approx 2.2 \times 10^{-22} \text{ mag}/(\text{H cm}^{-2})$. However, it is also clear from Fig. 17 that values of $\frac{A_V}{N_H}$ are generally higher around the selected regions than the values derived from a global analysis at an equivalent distance from 30 Dor.

The X_{CO} values for the individual regions vary from 0.5 to $7 \times 10^{20} \text{ H}_2 \text{ cm}^{-2}/(\text{K km s}^{-1})$, with an ensemble average value of $1.7 \times 10^{20} \text{ H}_2 \text{ cm}^{-2}/(\text{K km s}^{-1})$. The X_{CO} values show

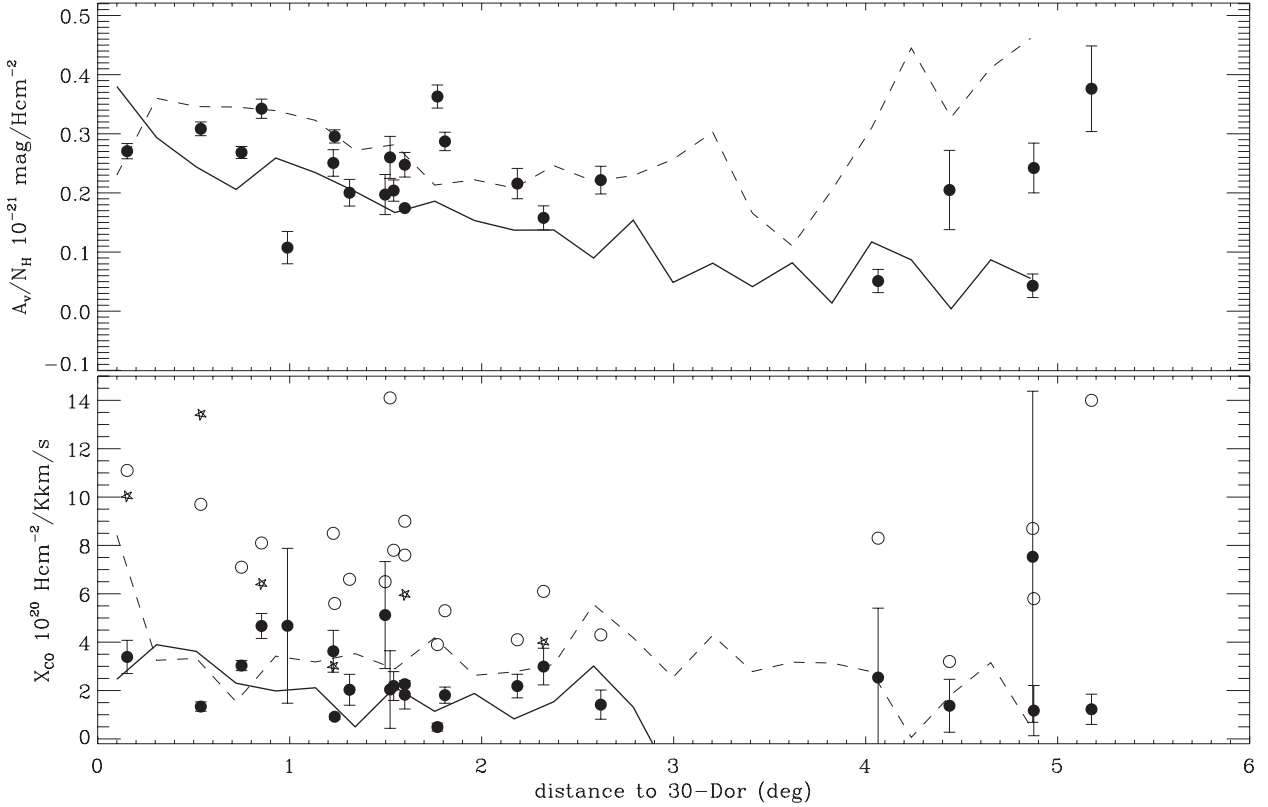


Fig. 17. Distribution of the parameters $\frac{A_V}{N_H}$ and X_{CO} derived from the fits of the correlation between the extinction data and the HI and CO gas tracers. The filled circles show the results for the individual molecular clouds in our sample. The open circles show the X_{CO} values derived from a virial analysis of the NANTEN CO data. The error bars shown are $\pm 3\sigma$ values. The thick solid lines show the parameters derived from the global correlation analysis of the extinction data, plotted as a function of distance to the 30 Dor H II region. The broken lines show the result of a similar correlation analysis performed on the Spitzer FIR emission at $160 \mu\text{m}$, using a τ^{160}/τ^V ratio derived for the solar neighborhood in order to scale the results to A_V (see Sect. 3.5).

a large dispersion, with values considerably above and below the Galactic value. Nonetheless, the ensemble average value ($X_{CO} = 1.76 \times 10^{20} \text{ H}_2 \text{ cm}^{-2}/(\text{K km s}^{-1})$) is similar to the MW value. The value of X_{CO} derived using a virial analysis by Fukui et al. (2008) is approximately three times greater than the average value derived using our extinction method. Part of this discrepancy may be due to systematic errors in the virial estimate of X_{CO} , since the method relies on accurately measuring the size and linewidth of the molecular clouds and hence may be affected by insufficient angular resolution to resolve clouds at the distance of the LMC, by noise or by the algorithm used to identify the molecular clouds. However, higher angular resolution ($HPBW \sim 45''$) observations of molecular clouds in the LMC by the Swedish-ESO Submillimetre Telescope suggest an average virial estimate for X_{CO} of $4.3 \pm 0.6 \times 10^{20} \text{ H}_2 \text{ cm}^{-2}/(\text{K km s}^{-1})$ (Israel et al. 2003). At least part of the discrepancy between the extinction and virial estimates of X_{CO} therefore seems real. In Fig. 19, we compare the extinction-based and L_{CO} -averaged virial X_{CO} values for each region. These values are also tabulated in Table 2. Figure 19 clearly shows that our estimates of X_{CO} based on extinction are lower than the values derived from a virial analysis for most clouds. Note however that our extinction-based values of X_{CO} are not independent of our adopted values for $\frac{A_V}{N_H}$, as discussed in Sect. 3.2. If, instead of determining $\frac{A_V}{N_H}$ locally for each region, we use a constant value derived from the correlation analysis in the outer regions of the LMC ($\frac{A_V}{N_H} = 0.63 \times 10^{-22} \text{ mag}/(\text{H cm}^{-2})$), we obtain the X_{CO} values

listed as X_{CO}^{ref} in Table 2 ($X_{CO}^{\text{ref}} = X_{CO} * \frac{A_V}{N_H}/0.63 \times 10^{-22}$). The X_{CO}^{ref} values are much closer to the X_{CO} values derived from a virial analysis of the NANTEN data, with an average offset of only 20%. The validity of this approach is discussed in Sect. 4.

3.5. Comparison with IR emission

The correlation between dust and gas in the LMC, derived in this paper from extinction, is quite similar to what has recently been found from an analysis of Spitzer observations of the FIR emission (Bernard et al. 2008). These authors showed that the correlation between the FIR emission and the HI column density is non-linear, with the emissivity at $160 \mu\text{m}$ (τ^{160}/N_H) increasing from low values in the low column density outer regions of the LMC to much higher values in the vicinity of the two molecular clouds LMC-154 and LMC-216. Note that these two clouds are included among the regions that analyzed in detail in this paper. Both clouds are well-detected in our extinction map, which allows a direct comparison between the dust properties inferred from absorption and emission. Bernard et al. (2008) derived dust abundance in the atomic medium surrounding these clouds. Using BG dust abundances in their Table 2 for case #2, and rescaling to the MW diffuse values (for which $\tau^{160}/N_H = 2.44 \times 10^{-25} \text{ cm}^2$ is assumed), we derive $\tau^{160}/N_H = 1.48 \times 10^{-25} \text{ cm}^2$ and $2.35 \times 10^{-25} \text{ cm}^2$ for LMC-154 and LMC-216 respectively. Using the values of $\frac{A_V}{N_H}$ for these two clouds listed in our Table 2, we find that the ratio of FIR to visual extinction, τ^{160}/τ^V , is

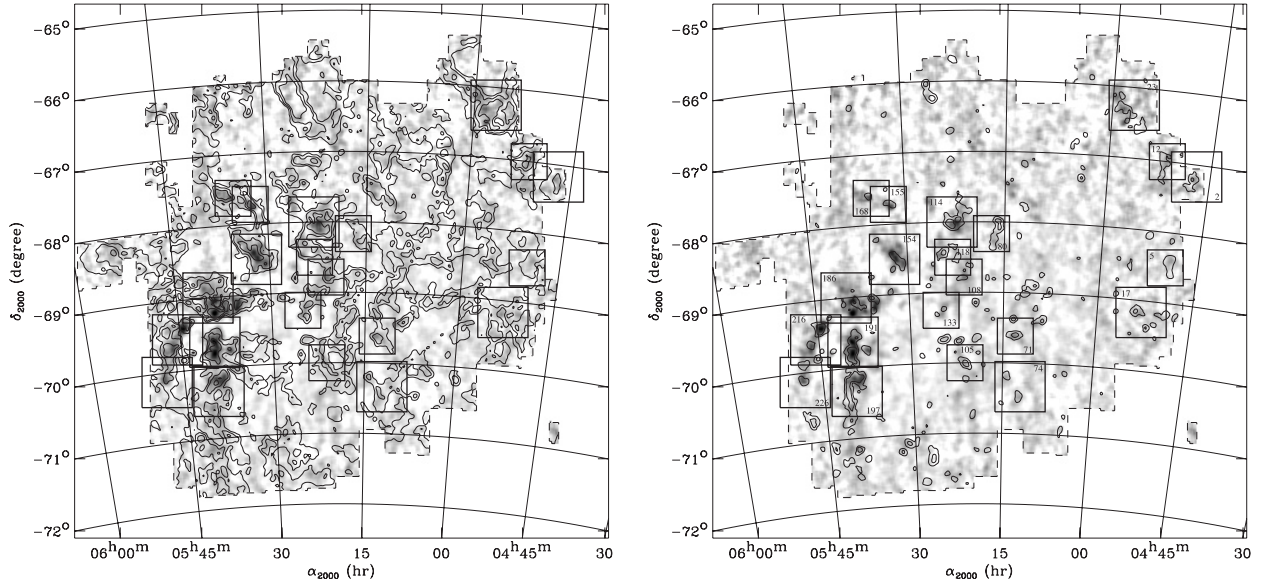


Fig. 18. Extinction map of the LMC (grayscale) overlaid with the H I integrated intensity contours (*left*), and the CO integrated intensity of the NANTEN survey (*right*). Both the CO and H I maps are filtered in the same way as the A_V map. Contours are set to 1000 and 5000 K km s⁻¹ for the H I map and 1 and 4 K km s⁻¹ for the CO map. The dashed line shows the field-of-view of the Nagoya Survey. The square boxes show the individual regions considered in this study. The labels on the right panel correspond to the names of the regions listed in Table 1.

Table 1. CO parameters of the regions studied in this paper. Columns 1–3 give the region name and centre coordinates respectively. Columns 4–6 give the average L_{CO} , M_{vir} and X_{CO} of CO clouds falling in each region. The average values are computed from the values in Fukui et al. (2008), using L_{CO} of each cloud as a weight. Column 7 gives the cloud numbers falling in each region.

Region	α_{2000}	δ_{2000}	$\langle L_{CO} \rangle / 10^4$ K km s ⁻¹ pc ²	$\langle M_{vir} \rangle / 10^4$ M_{\odot}	$\langle X_{CO} \rangle / 10^{20}$ H ₂ cm ⁻² / (K km s ⁻¹)	CO clouds ^a
LMC-186	5h40m00s	-69°00' 0"	2.99	70.5	11.3	183, 186, 189, 201, 204, 261, 268
LMC-191	5h39m30s	-69°38' 0"	2.26	51.4	9.6	181, 182, 184, 191, 206, 207, 260, 266, 268
LMC-216	5h45m30s	-69°33' 0"	9.00	134.0	6.9	206, 207, 216, 217, 220, 223, 226, 266, 268
LMC-154	5h32m00s	-68°30' 0"	5.11	70.0	8.0	150, 154, 157, 163, 164, 172, 256
LMC-133	5h25m00s	-69°15' 0"	0.41	9.3	8.8	124, 133
LMC-197	5h39m30s	-70°20' 0"	69.5	841.0	5.6	188, 197, 262, 263
LMC-226	5h48m00s	-70°08' 0"	2.35	33.6	6.8	220, 226, 227, 270
LMC-155	5h32m30s	-67°43' 0"	2.70	3.83	6.5	155, 257
LMC-168	5h35m00s	-67°37' 0"	2.40	47.2	9.7	155, 168, 257
LMC-118	5h23m00s	-68°30' 0"	3.29	44.6	7.8	112, 118, 125, 128
LMC-108	5h21m15s	-68°47' 0"	1.57	28.2	7.6	101, 108
LMC-105	5h21m15s	-70°00' 0"	5.00	4.38	4.1	104, 105, 92
LMC-114	5h23m00s	-68°00' 0"	18.7	217.0	6.3	107, 114, 118, 138
LMC-80	5h17m00s	-68°10' 0"	13.0	120.0	4.1	80
LMC-71	5h13m00s	-69°37' 0"	4.84	57.3	5.0	65, 71, 72, 244
LMC-74	5h12m00s	-70°20' 0"	2.33	21.5	4.3	69, 74, 77
LMC-17	4h53m00s	-69°10' 0"	3.54	58.9	8.3	10, 11, 14, 17, 18, 21, 234
LMC-5	4h50m00s	-68°30' 0"	7.50	52.9	3.2	5
LMC-23	4h57m00s	-66°15' 0"	2.92	55.7	8.7	23, 30, 31, 32, 33, 35, 236
LMC-12	4h51m30s	-67°00' 0"	5.35	64.6	5.8	7, 12
LMC-2	4h47m00s	-67°10' 0"	6.50	204.0	13.7	2, 7, 231, 232

^a Cloud numbers from Fukui et al. (2008).

4.7×10^{-4} and 9.5×10^{-4} for LMC-154 and LMC-216 respectively. In the solar neighborhood, a reference value can be calculated using $\left(\frac{A_V}{N_H}\right)_{SN} = 5.34 \times 10^{-22}$ mag/(H cm⁻²) (see Sect. 2.4) and a reference dust emissivity value of $\left(\tau^{160}/N_H\right)_{SN} = 2.44 \times 10^{-25}$ cm² (Boulanger et al. 1996), assuming an emissivity index for the dust of $\beta = 2$. The solar neighborhood value derived in this way is $\left(\tau^{160}/\tau^V\right)_{SN} = 4.9 \times 10^{-4}$, which is similar to the value derived for cloud LMC-154, and a factor of ~ 2.0 lower than that derived for LMC-216.

We performed a global comparison of the dust properties inferred from emission and absorption using the 160 μ m map of Bernard et al. (2008) and the set of annuli described in Sect. 3.3. The results are shown in Fig. 17. The derived τ^{160}/N_H values were rescaled to the A_V scale using the reference value $\left(\tau^{160}/\tau^V\right)_{SN}$ calculated above. It can be seen that the two curves match reasonably well in the inner regions of the LMC. Combined with the good correspondence obtained for LMC-154 and LMC-216, this indicates that the overall cross-section variations from FIR to visible wavelengths are rather similar for LMC

Table 2. Parameters derived in this study, for the whole LMC and the individual regions selected. Column 2 gives the extinction to column density ratio. Column 3 gives the apparent CO-to-H₂ conversion factor. Errors on the parameters are 1- σ values. Column 4 gives the reduced χ^2 of the linear correlation. Column 5 gives the L_{CO} -averaged X_{CO} factor derived from virial analysis for each region. Column 6 compares this value to that of Col. 3. Column 7 gives the X_{CO} derived from our study using a constant $\frac{A_V}{N_{\text{H}}}$ ratio of 0.63×10^{-22} mag/(H cm⁻²), as derived in external regions of the LMC. Column 8 compares this estimate to the Virial value.

Region	$\frac{A_V}{N_{\text{H}}}/10^{-22}$ mag/(H cm ⁻²)	$X_{\text{CO}}/10^{20}$ H ₂ cm ⁻² /(K km s ⁻¹)	χ^2 –	$X_{\text{CO}}^{\text{vir}}/10^{20}$ H ₂ cm ⁻² /(K km s ⁻¹)	$X_{\text{CO}}^{\text{Vir}}/X_{\text{CO}}$ –	$X_{\text{CO}}^{\text{Ref}}/10^{20}$ H ₂ cm ⁻² /(K km s ⁻¹)	$X_{\text{CO}}^{\text{Vir}}/X_{\text{CO}}^{\text{Ref}}$ –
AllLMC	1.74 ± 0.01	2.26 ± 0.05	0.93	7.00	3.10	6.24	1.12
LMC-186	2.71 ± 0.09	3.39 ± 0.46	1.41	11.10 ± 2.00	3.28	14.51	1.31
LMC-191	3.08 ± 0.08	1.34 ± 0.13	1.58	9.70 ± 2.80	7.26	6.52	0.67
LMC-216	2.68 ± 0.07	3.03 ± 0.14	1.43	7.10 ± 2.90	2.34	12.88	1.81
LMC-154	3.42 ± 0.11	4.67 ± 0.34	1.03	8.10 ± 8.00	1.73	25.30	3.12
LMC-133	2.51 ± 0.15	3.62 ± 0.58	1.23	8.50 ± 5.00	2.35	14.37	1.69
LMC-197	2.96 ± 0.07	0.92 ± 0.07	2.01	5.60 ± 1.10	6.11	4.28	0.76
LMC-226	2.00 ± 0.15	2.03 ± 0.43	0.74	6.60 ± 1.00	3.25	6.44	0.98
LMC-155	1.97 ± 0.23	5.12 ± 1.47	0.56	6.50	1.27	15.98	2.46
LMC-168	2.60 ± 0.24	2.04 ± 1.07	0.78	14.10 ± 4.30	6.90	8.40	0.60
LMC-118	2.04 ± 0.12	2.19 ± 0.40	1.61	7.80 ± 7.00	3.57	7.06	0.91
LMC-108	2.48 ± 0.14	1.83 ± 0.39	1.16	7.60 ± 1.70	4.16	7.15	0.94
LMC-712	3.63 ± 0.13	0.49 ± 0.11	1.27	3.90 ± 0.50	7.99	2.80	0.72
LMC-114	2.87 ± 0.10	1.81 ± 0.22	0.94	5.30 ± 2.00	2.93	8.21	1.55
LMC-80	2.16 ± 0.17	2.19 ± 0.33	1.39	4.10	1.88	7.46	1.82
LMC-71	1.58 ± 0.14	2.99 ± 0.51	0.93	6.10 ± 2.80	2.04	7.47	1.22
LMC-74	2.22 ± 0.16	1.42 ± 0.40	0.71	4.30 ± 0.60	3.04	4.97	1.16
LMC-17	0.51 ± 0.13	2.54 ± 1.91	0.73	8.30 ± 8.80	3.27	2.05	0.25
LMC-5	2.05 ± 0.45	1.37 ± 0.73	0.58	3.20	2.34	4.44	1.39
LMC-23	0.43 ± 0.13	7.53 ± 4.56	0.97	8.70 ± 2.60	1.16	5.12	0.59
LMC-12	2.42 ± 0.28	1.17 ± 0.69	0.71	5.80 ± 1.50	4.96	4.48	0.77
LMC-2	3.76 ± 0.48	1.22 ± 0.42	0.79	14.00 ± 0.90	11.44	7.28	0.52
ens. average	2.54 ^d	1.39 ^d	–	7.45	3.96	8.43	1.20

^d Computed with a weight inversely proportional to square of errors.

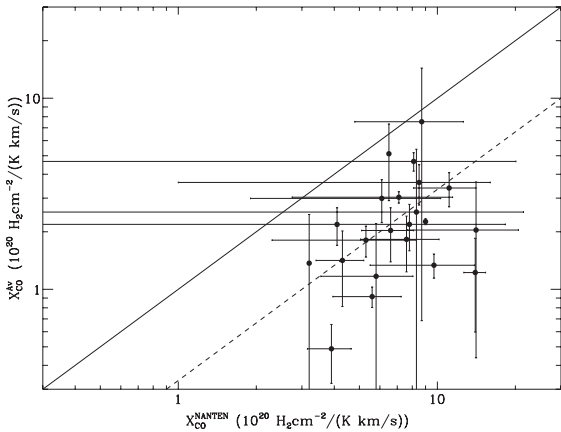


Fig. 19. Comparison between the X_{CO} values derived from a virial analysis of the NANTEN CO data ($X_{\text{CO}}^{\text{NANTEN}}$, horizontal axis) with values derived here ($X_{\text{CO}}^{\text{AV}}$, vertical axis) for our sample of individual clouds. The solid and broken lines indicate $X_{\text{CO}}^{\text{AV}} = X_{\text{CO}}^{\text{NANTEN}}$ and $X_{\text{CO}}^{\text{AV}} = \frac{1}{3} X_{\text{CO}}^{\text{NANTEN}}$, respectively.

and solar neighborhood dust, consistent with similar dust composition and optical properties.

4. Discussion

Our results indicate a trend such that the apparent dust absorptivity $\frac{A_V}{N_{\text{H}}}$ increases systematically from the outer regions of the LMC to the region surrounding the massive star-forming region

30 Dor. Also, the extinction-based CO-to-H₂ conversion factor, X_{CO} , is much lower than the value derived from a virial analysis of CO data.

In principle, the observed variations of $\frac{A_V}{N_{\text{H}}}$ could be due to varying optical properties of dust grains at NIR wavelengths. However, as discussed in Sect. 3, the reasonable amplitude of such variations should not strongly affect the derived extinction, and the variations should in any case be much smaller than what is observed even if extreme processes such as grain-grain coagulation are invoked. Some of the variations observed – in particular, the increase of the FIR emissivity for several individual clouds at the periphery of the LMC shown in Fig. 17 – could be due to dust aggregation in those close, as the outer regions of the LMC are the coldest (Bernard et al. 2008).

Our results could also be explained by intrinsic variations of the dust-to-gas ratio across the LMC. The observed variations of $\frac{A_V}{N_{\text{H}}}$ would then suggest that dust is more abundant in the inner LMC and in the vicinity of molecular clouds than in the outskirts of the LMC. Since star formation takes place in molecular clouds, this in turn could be explained as a variation in the local metallicity associated with star formation. The fact that $\frac{A_V}{N_{\text{H}}}$ is higher around molecular clouds might indicate that there are dust abundance variations caused by metallicity variations associated with present and past star formation activity in the LMC, with dust being more abundant close to major star formation sites such as 30 Dor. However, this interpretation leads to the X_{CO} values that are several times lower than those derived from a virial analysis of the NANTEN CO data. This would lead to the conclusion that the clouds are not in virial equilibrium but are either transient expanding structures, or are kept in dynamic

equilibrium due to significant external pressure in the ambient medium. We note that the virial masses adopted here are derived under the assumption of no external pressure and magnetic field support, as $M_{\text{vir}} \propto R\Delta V^2$ where R and ΔV are the cloud radius and the CO linewidth. If the clouds are in gravitational equilibrium in the presence of high external pressure, the virial mass calculated in this manner would overestimate the true cloud mass by a factor of two at most. Neglecting the possibility of support against gravitational collapse by the cloud's magnetic field, the cloud parameters (i.e., R and ΔV) determined by Fukui et al. (2008) suggest that an external pressure of only $P/k \sim 10^3\text{--}10^4 \text{ K cm}^{-3}$ would allow the measured M_{vir} to exceed the true cloud mass by a factor of two for many of the clouds in our sample, which would largely account for the discrepancy between the extinction and virial estimates of the X_{CO} factor.

As discussed by Bernard et al. (2008) in relation to the dust emissivity, variations of $\frac{A_V}{N_{\text{H}}}$ and τ^{160}/N_{H} might also be due to the association of dust with an additional gas component that is not detected by the available gas tracers. Both the extinction and FIR emission studies suggest that this component should be strongly correlated with the HI distribution. From an analysis of Spitzer FIR data for the LMC, Bernard et al. (2008) showed that the mass of this component must be twice the mass detected in HI, or 20 times the mass of the molecular phase as deduced from the CO emission. This additional gas component could be composed of pure H_2 with no CO, or optically thick HI emission. Molecular hydrogen without CO emission has been identified through excess IR emission in the solar neighborhood, and is thought to be more dominant in low metallicity objects such as the SMC (see Leroy et al. 2007) and other local dwarf galaxies (e.g., Madden et al. 1997), where the low dust abundance promotes the photodissociation of CO molecules. In the LMC, however, Bernard et al. (2008) has shown that this component could also be due to self-absorption of the 21 cm emission by cold HI. In both cases, we would expect the additional gas component to be preferentially located around CO-emitting clouds, and to increase from the outer regions of the LMC to the inner regions. The dust absorption associated with the additional gas component would lead to an overestimate of $\frac{A_V}{N_{\text{H}}}$ in our correlation analysis, and thus an underestimate of X_{CO} . A factor of two increase in N_{H} due to an additional gas component would reduce our derived values of X_{CO} by a factor of three. If we were to assume that the external regions of the LMC that show the lowest $\frac{A_V}{N_{\text{H}}}$ values correspond to regions where the extra gas component is negligible compared to the gas mass that is accurately traced by the HI emission, and that the dust abundance does not vary across the LMC, it would be reasonable to adopt a fixed value of $\frac{A_V}{N_{\text{H}}} = 0.63 \times 10^{-22} \text{ mag}/(\text{H cm}^{-2})$ for the entire LMC. We have shown that the values of X_{CO} derived under these hypotheses are consistent, on average, with the values derived from a virial analysis of the CO data (see e.g., Table 2), although some region-to-region dispersion remains. These region-to-region variations could either be due to uncertainties in the virial estimate, or to deviations in the gas-to-dust ratio. It is worth noting that the proposed additional gas component, should it exist, would also be a source of high external pressure at the ‘‘surface’’ of CO-emitting volume of a molecular cloud, which would contribute to an overestimation of the cloud's virial mass, as discussed above.

Note that under the hypothesis of an extra gas component and constant gas-to-dust ratio, the adopted value of $\frac{A_V}{N_{\text{H}}}$ is 8.5 times lower than in the solar neighborhood. This would suggest a somewhat non-linear relationship between metallicity and

dust abundance, since the metallicity of the LMC is at least 1/3 solar. It should also be noted, however, that the dust abundance derived here using extinction data is significantly lower than the abundance derived from the FIR emission (lower than in the solar neighborhood by a factor of 2.7, Bernard et al. 2008). The reason for this discrepancy is not clear, but may be due to an artifact of the extinction map. A possible explanation is that the extinction map does not trace the dust distribution faithfully at low column densities, due to the filtering applied. On the other hand, if the observed variations are due to genuine changes in the dust abundance in the LMC, then the average dust abundance derived around the CO clouds ($\frac{A_V}{N_{\text{H}}} = 2.45 \times 10^{-22} \text{ mag}/(\text{H cm}^{-2})$) corresponds to a dust abundance only 2.1 times lower than in the solar neighborhood, suggesting a linear relationship between dust abundance and metallicity.

Finally, we note that the results of this paper seem to disagree with the global X_{CO} estimate obtained by Imara & Blitz (2007). These authors also constructed an extinction map of the LMC using the 2MASS catalog, and their map resembles the one presented here both in amplitude and morphology. Imara & Blitz (2007) did not perform a correlation analysis, but instead subtracted the HI contribution from the total N_{H} derived from the extinction using a single value of $\frac{A_V}{N_{\text{H}}} = 1.5 \times 10^{-22} \text{ mag}/(\text{H cm}^{-2})$, under the statistical assumption that only half the HI emission will show up in extinction. The average extinction measured by Imara & Blitz (2007) towards CO-bright regions suggests an average value of $X_{\text{CO}} = 9.3 \pm 0.4 \times 10^{20} \text{ H}_2 \text{ cm}^{-2}/(\text{K km s}^{-1})$ across the LMC, somewhat larger than the recent virial estimate by Fukui et al. (2008). We note that if we had assumed their value for $\frac{A_V}{N_{\text{H}}}$ for our analysis, we would have deduced a much smaller ensemble average X_{CO} value of $3.55 \times 10^{20} \text{ H}_2 \text{ cm}^{-2}/(\text{K km s}^{-1})$. However, it must also be noted that their implied definition of the H_2 column density entering X_{CO} is the total H_2 column density along the line of sight ($X_{\text{CO}}^{\text{tot}}$), whereas our definition – and the definition assumed by the virial analysis – refers only to the fraction of the H_2 column density associated with the CO-emitting gas ($X_{\text{CO}}^{\text{loc}}$, see discussion in Sect. 3.2). If, on average, an extra gas component contributes twice the HI column density (see Bernard et al. 2008), the two definitions of X_{CO} are related by $X_{\text{CO}}^{\text{tot}} = X_{\text{CO}}^{\text{loc}}(1 + 2 \times N_{\text{H}}^{\text{HI}}/N_{\text{H}}^{\text{CO}})$ where N_{H}^{HI} and N_{H}^{CO} are the total column density towards the cloud in the HI and CO phases. For most of the molecular regions selected for our correlation analysis, the ratio $N_{\text{H}}^{\text{HI}}/N_{\text{H}}^{\text{CO}}$ is close to unity (ensemble average $\langle N_{\text{H}}^{\text{HI}}/N_{\text{H}}^{\text{CO}} \rangle = 0.77$). Taking this difference into account, our estimate and the Imara & Blitz (2007) estimate for the average X_{CO} in the LMC are in fact quite consistent.

5. Conclusion

We used 2MASS data to construct a map of the visual extinction (A_V) in the Large Magellanic Cloud (LMC). Using this A_V map, we measured the dust abundance $\frac{A_V}{N_{\text{H}}}$ as well as the X_{CO} factor in the LMC. The main results of our analysis are the following:

- (1) We developed a new method to measure the color excess due to dark clouds. The well-known NICE method uses the mean color of stars located in a cell placed over the cloud surface, whereas our new method utilizes the color of the X percentile reddest star. The new method is robust against contamination by foreground stars, which often leads to an underestimate of the true extinction in the case of the

traditional NICE method. The new method also yields an estimate of the cloud's position relative to the stellar distribution along the line of sight.

- (2) We applied our new method to the 2MASS point source catalog to derive an A_V map of the LMC. The resulting A_V map is similar to the integrated intensity of the CO emission, as observed by the NANTEN telescope. However, there are some clouds that escaped detection in the A_V map that are well-detected in CO. Comparison between the A_V map and model calculations indicates that such clouds are probably located towards the back of the LMC's stellar distribution. On the contrary, clouds that are well-detected both in CO and A_V are inferred to be located towards the front of the stellar distribution.
- (3) We conducted a correlation analysis across the LMC, and for a sample of 21 regions that are detected in both the A_V and CO maps. Assuming that the dust has similar IR absorption properties in both the atomic and molecular phases, we derived the ratio of dust absorption to gas column density ($\frac{A_V}{N_{\text{H}}}$), and the ratio of the integrated CO line intensity to the H_2 column density (X_{CO}). We have shown that the apparent dust absorptivity increases from the outskirts of the LMC towards the 30 Dor star forming region. This can be explained either by: i) a systematic increase of the dust abundance in the proximity of star forming regions; or ii) by the presence of an additional gas component that is not traced by the HI or CO emission, and that is strongly correlated with the HI distribution. Both possible explanations may be at work. The X_{CO} values that we derive from our extinction maps are much smaller than the values inferred from a virial analysis of the CO data. Under hypothesis i), this implies that clouds are either not in virial equilibrium or that they are maintained by substantial external pressure. Under these same assumptions, the inferred dust abundance in the LMC varies spatially, from 8.5 to 2 times lower than the solar neighborhood value from the periphery to the inner regions of the galaxy. Under hypothesis ii), our derived X_{CO} values can be reconciled with the virial estimates assuming a constant dust abundance that is 8.5 times lower than in the solar neighborhood, and an additional gas component with approximately twice the mass of the component traced by the HI emission. These conclusions generally agree with the conclusions determined from an analysis of the FIR emission in the LMC, although the dust abundance in the outskirts of the LMC derived from our extinction map is significantly lower, which may reflect a bias in the method used to derive the extinction map against low column densities.

Acknowledgements. This work was supported by a "Poste Rouge" from Observatoire Midi-Pyrénées, and also by Grants-in-Aid for Scientific Research from JSPS (17540214), MEXT (18026003), and Ito Science Society (H19). This publication makes use of data products from the Two Micron All Sky Survey, which is a joint project of the University of Massachusetts and the Infrared Processing and Analysis Center/California Institute of Technology, funded by

the National Aeronautics and Space Administration and the National Science Foundation.

References

- Abergel, A., Boulanger, F., Mizuno, A., & Fukui, Y. 1994, *ApJ*, 423, L59
 Alves, J., Lada, C. J., Lada, E. A., Kenyon, S. J., & Phelps, R. 1998, *ApJ*, 506, 292
 Bernard, J.-Ph., Boulanger, F., & Puget, J. L. 1993, *A&A*, 277, 609
 Bernard, J.-Ph., Abergel, A., Ristorcelli, I., et al. 1999, *A&A*, 347, 640
 Bernard, J.-Ph., Reach, W., Paradis, D., et al. 2008, *AJ*, submitted
 Bessell, M. S., & Brett, J. M. 1998, *PASP*, 100, 1134
 Bohlin, R. C., Savage, B. D., & Drake, J. F. 1978, *ApJ*, 224, 132
 Boulanger, F., Falgarone, E., Puget, J. L., & Helou, G. 1990, *A&A*, 364, 136
 Boulanger, F., Abergel, A., Bernard, J.-P., et al. 1996, *A&A*, 312, 256
 Bot, C., Boulanger, F., Lagache, G., Cambrésy, L., & Egret, D. 2004, *A&A*, 423, 567
 Cambrésy, L. 1999, *A&A*, 345, 965
 Cambrésy, L., Beichman, C. A., Jarrett, T. H., & Cutri, R. M. 2002, *AJ*, 123, 2559
 Cambrésy, L., Jarrett, T. H., & Beichman, C. A. 2005, *A&A*, 435, 131
 Cardelli, J. A., Clayton, G. C., & Mathis, J. S. 1989, *ApJ*, 345, 245
 Davidge, T. J. 2003, *ApJ*, 597, 289
 Dobashi, K., Bernard, J.-Ph., Yonekura, Y., & Fukui, Y. 1994, *ApJS*, 95, 419
 Dobashi, K., Uehara, H., Kandori, R., et al. 2005, *PASJ*, 57, S1
 Dufour, R. J. 1984, in *Structure and evolution of the Magellanic Clouds*, ed. S. van den Bergh, & K. S. de Boer (Dordrecht: Reidel), IAU Symp., 108, 353
 Dupac, X., Giard, M., Bernard, J.-Ph., et al. 2002, *A&A*, 392, 691
 Dupac, X., Bernard, J.-Ph., Boudet, N., et al. 2003, *A&A*, 404, L11
 Feast, M. 1999, *PASP*, 761, 775
 Fukui, Y., Kawamura, A., Minamidani, T., et al. 2008, *ApJ*, in press
 Galliano, F., Madden, S. C., Jones, A. P., et al. 2003, *A&A*, 407, 159
 Gordon, K. D., Clayton, G. C., Misselt, K. A., Landolt, A. U., & Wolff, M. J. 2003, *ApJ*, 594, 279
 Imara, N., & Blitz, L. 2007, *ApJ*, 662, 969
 Israel, F. P., Johansson, L. E. B., Rubio, M., et al. 2003, *A&A*, 406, 817
 Kandori, R., Dobashi, K., Uehara, H., Sato, F., & Yanagisawa, K. 2003, *AJ*, 126, 1888
 Keller, S. C., & Wood, P. R. 2006, *ApJ*, 642, 834
 Kim, S., Staveley-Smith, L., Dopita, M. A., et al. 2003, *ApJS*, 148, 473
 Lada, C. J., Lada, E. A., Clemens, D. P., & Bally, J. 1994, *ApJ*, 429, 694
 Laureijs, R. J., Clark, F. O., & Prusti, T. 1991, *ApJ*, 372, 185
 Leroy, A., Bolatto, A., Stanimirovic, S., et al. 2007, *ApJ*, 658, 1027
 Lombardi, M., & Alves, J. 2001, *A&A*, 377, 1023
 Luhman, K. L., Whitney, B. A., Meade, M. R., et al. 2006, *ApJ*, 647, 1180
 Madden, S. C., Poglitsch, A., Geis, N., Stacey, G. J., & Townes, C. H. 1997, *ApJ*, 483, 200
 Meixner, M., Gordon, K. D., Karl, D., et al. 2006, *AJ*, 132, 2268
 Miville-Deschênes, M.-A., Boulanger, F., Joncas, G., & Falgarone, E. 2002, *A&A*, 381, 209
 Mizuno, N., Yamaguchi, R., Mizuno, A., et al. 2001, *PASJ*, 53, 971
 Ossenkopf, V. 1993, *A&A*, 280, 617
 Rieke, G. M., & Lebofsky, M. J. 1985, *ApJ*, 288, 618
 Sakon, I., Onaka, T., Kaneda, H., et al. 2006, *ApJ*, 651, 174
 Sauvage, M., Vigroux, L., & Thuan, T. X. 1990, *A&A*, 237, 296
 Staveley-Smith, L., Kim, S., Calabretta, M. R., et al. 2003, *MNRAS*, 339, 87
 Stepnik, B., Abergel, A., Bernard, J.-Ph., et al. 2003, *A&A*, 398, 551
 Strong, A. W., & Mattox, J. R. 1996, *A&A*, 308, L21
 Tsalmantza, P., Kontizas, E., Cambresy, L., et al. 2006, *A&A*, 447, 89
 Westerlund, B. E. 1997, *The Magellanic Clouds* (New York: Cambridge Univ. Press)
 Zaritsky, D., Harris, J., Thompson, I. B., & Grebel, E. K. 2004, *AJ*, 128, 1606